Optimizing PPP Performance by Incorporating ZWD Constraints Derived from Data Assimilation

Dehvari, Masoud; Farzaneh, Saeed; Forootan, Ehsan

Published in:
Earth and Space Science

DOI (link to publication from Publisher):
10.1029/2024EA004173

Publication date:
2025

Document Version
Accepted author manuscript, peer reviewed version

Optimizing PPP Performance by Incorporating ZWD Constraints Derived from Data Assimilation

Masoud Dehvari[1], Saeed Farzaneh[1*], Ehsan Forootan[2]

[1]School of Surveying and Geospatial Engineering, College of Engineering, University of Tehran, Tehran, Iran.

[2]Geodesy Group, Department of Sustainability and Planning, Aalborg University, Rendburggade 14, 9000 Aalborg, Denmark.

Corresponding author: Saeed Farzaneh (Farzaneh@ut.ac.ir)

Key Points:

- A Calibration and Data Assimilation (C/DA) approach is proposed to enhance Zenith Wet Delay (ZWD) estimation using the Ensemble Kalman Filter (EnKF).
- Estimated ZWD values from the C/DA method are incorporated as constraints in the PPP method (PPP-DA).
- The PPP-DA method achieves a 21% reduction in 3D positioning errors and a 16% decrease in convergence times compared to conventional PPP techniques.

Abstract

One of the primary error sources limiting the performance of the Precise Point Positioning (PPP) technique is the atmospheric wet delay, caused by the presence of water vapor in the lower atmosphere. Accurately representing this parameter is crucial for improving the initialization and accuracy of satellite-based positioning techniques. However, existing empirical models have struggled to capture the severe spatial and temporal variations of this parameter, thereby limiting their effectiveness in high-precision applications. To address these challenges, this study introduces a sequential Calibration and Data Assimilation (C/DA) approach to enhance the estimation and prediction of Zenith Wet Delay (ZWD) values. For this aim, an empirical regional atmospheric wet delay model was constructed using Principal Component Analysis (PCA), serving as the background model for the C/DA method. The methodology involves calibrating this empirical ZWD model using the Ensemble Kalman Filter (EnKF) method, wherein observed ZWD values from approximately 309 GNSS stations across the central Europe are assimilated into the model. The calibrated model parameters were then used to estimate ZWD values, which were subsequently applied as constraints in the PPP method (referred to as PPP-DA) at 10 GNSS test stations within the study area. The study compares the positioning accuracy and convergence

time achieved using the PPP-DA method with those obtained from traditional PPP approaches and PPP utilizing ZWD constraints from the GFS model (PPP-GFS). The results demonstrate a significant enhancement, with the PPP-DA method achieving an average improvement of 2 millimeters in positioning accuracy across all considered stations (representing a 21% reduction compared to the conventional PPP method), along with an average decrease in convergence time of approximately 16%. These findings highlight the potential of integrating C\DA techniques to refine the accuracy and efficiency of satellite-based positioning.

Plain Language Summary

The accuracy of satellite-based positioning systems, such as those used in navigation and geodesy, can be significantly impacted by atmospheric wet delay caused by water vapor. This delay affects how signals travel through the atmosphere, particularly in high-precision applications. Existing models struggle to account for rapid and complex changes in atmospheric water vapor. In this study, we developed a new approach combining Calibration and Data Assimilation (C/DA) techniques to better estimate Zenith Wet Delay (ZWD), which represents the effect of atmospheric water vapor on satellite signals. By integrating data from Global Navigation Satellite System (GNSS) observations with a proposed regional atmospheric model, our method improves both the accuracy and efficiency of ZWD estimation. When incorporated as constraints in the PPP method, the proposed approach significantly improved positioning accuracy and reduced initialization times, highlighting its potential to enhance satellite-based applications.

1. Introduction

Precise Point Positioning (PPP) has become a widely adopted technique within the Global Navigation Satellite System (GNSS) community, known for its single-receiver capability, global coverage, robust processing error mitigation (Wilgan et al., 2017). Despite its advantages, PPP, especially in real-time applications, faces challenges, notably the long initialization time required to achieve centimeter-level positioning accuracy. This limitation is primarily due to the ionospheric-free linear combination used in PPP, which transforms carrier-phase ambiguities from integer values into float values, complicating their resolution and extending the convergence time. Additionally, in precise GNSS positioning, resolving station height and atmospheric delay simultaneously can be challenging, particularly because the strong correlation between tropospheric wet delay and station height can lead to parameter coupling during the estimation process. This coupling complicates the separation of these parameters and may increase the time required to achieve sub-decimeter positioning accuracy (Kouba & Héroux, 2001).

Tropospheric wet delay, caused by the presence of water vapor in the lower atmosphere, is a major error source that significantly impacts the performance of GNSS positioning. Highly accurate tropospheric corrections offer another pathway to reduce convergence time by fixing the tropospheric delay during PPP processing, thereby decreasing the number of unknown parameters (de Oliveira Jr et al., 2017; X. Li et al., 2011; Mirmohammadian et al., 2022; Wilgan et al., 2017; Yao et al., 2014). Previous researches have explored the integration of external tropospheric models into the PPP method. For instance, Yao et al. (2014) introduced a GNSS-

based global Zenith Total Delay (ZTD) model as a pseudo observation to this method, resulting in a 15% improvement in PPP convergence time. Similarly, de Oliveira et al. (2017) investigated the application of regional GNSS-based ZTD models in real-time kinematic PPP and reported improvements in convergence time. Their results showed reductions of approximately 1%, 20%, and 5% in the convergence time for the east, north, and up components, respectively. Additionally, Li et al. (2011) employed interpolated ZWD values from neighboring stations to enhance ambiguity fixing performance in the PPP method. Song et al. 2022 explored the integration of interpolated ZWD values, derived via the Kriging method, into the PPP-RTK framework. Their findings revealed that the tropospheric-weighted model achieved 3D convergence times of 25.5 minutes and 15 minutes for the ambiguity-float and ambiguity-fixed solutions, respectively. In contrast, the standard PPP-RTK model required 31.5 minutes and 18.5 minutes for the corresponding solutions. However, these approaches carry the risk of degrading the accuracy of the vertical component if the provided model does not accurately reflect real tropospheric conditions. Another approach to modeling ZWD values involves estimating them using tomography methods. For example, Haji-Aghajany et al. 2020 compared ZWD values derived from voxel-based and functional model tomography within a PPP experiment. Their findings indicated improvements of approximately 6 mm, 3 mm, and 9 mm in the east, north, and up components, respectively. However, the complexity of constructing the design matrix and addressing the inherently ill-posed nature of the tomography problem presents a significant challenge to the practical implementation of this method.

One approach to modeling this parameter is through the use of empirical atmospheric models (Collins & Langley, 1997; Landskron & Böhm, 2018). However, the parameters of these models are static, which limits their ability to capture only the low-frequency variations of wet atmospheric delay values (Dehvari et al., 2023, 2024a).

Recently, the advent of Numerical Weather Prediction (NWP) models with enhanced accuracy and spatial resolution has provided new opportunities for more precise tropospheric modeling, offering potential solutions for mitigating wet delay errors in GNSS applications (Boehm et al., 2006; Lu et al., 2017). Lu et al. (2017) demonstrated the benefits of using Zenith Wet Delay (ZWD) values derived from the Global Forecast System (GFS; National Centers for Environmental Prediction/National Weather Service/ NOAA/U.S. Department of Commerce, 2015), a global NWP model provided by the National Centers for Environmental Prediction (NCEP). Their findings indicated a 60% reduction in PPP convergence time and a 40% improvement in positioning accuracy. The use of Numerical Weather Prediction (NWP) models in PPP presents a promising alternative, as these models are available in near real-time with higher accuracy than empirical models. However, global NWP models typically suffer from low spatial and temporal resolution, which can limit their effectiveness in high-precision applications. To address these limitations, recent studies have proposed the use of regional NWP models, which offer higher spatial resolution (e.g., 4 km) and more frequent updates (e.g., hourly). Wilgan et al. (2017) applied Zenith Total Delay (ZTD) values derived from the Weather Research and Forecasting (WRF) model as constraints within the PPP method. Their findings showed that this approach reduced the average 3D positioning bias by 20 mm in static mode and 10 mm in kinematic mode. Additionally, using a high-resolution tropospheric model significantly decreased convergence time, reducing it from 67 to 58 minutes for horizontal components and from 79 to 63 minutes for the vertical component at the 10 cm convergence level. Moreover, (Gong et al., 2024) assessed the impact of Weather Research and Forecasting (WRF) model-based wet delay corrections on GNSS Precise Point Positioning (PPP) during two

observation periods in South China under varying weather conditions. By assimilating GNSS PWV data into the WRF model, vertical positioning accuracy improved by 14.6% to 33.7%, and convergence times were reduced by 25% to 48% for both static and kinematic PPP modes, demonstrating the effectiveness of WRF-enhanced corrections.

While the Weather Research and Forecasting (WRF) model provides high-resolution atmospheric data, its computational intensity and the need for extensive calibration and validation can be challenging. Additionally, the model's reliance on accurate initial conditions can lead to errors in tropospheric delay estimates if the input data is not precise (Skamarock et al., 2008).

Sequential Data Assimilation (DA) (Bertino et al., 2003) or Calibration and Data Assimilation (C/DA) (Forootan et al., 2024) methods utilize the uncertainties from both the background model and observations to deliver estimates with higher accuracy and reliability than those obtained from either source alone (Smith et al., 2013). This approach has been widely applied to calibrate empirical model parameters, addressing their limitations in capturing high-frequency variations. Dehvari et al. 2024b implemented a data assimilation approach using the Ensemble Kalman Filter (EnKF) to enhance the estimation of wet refractivity indices. GNSS-derived Zenith Wet Delay (ZWD) values were integrated into an empirical model, with wet refractivity indices represented as B-spline coefficients for efficient epoch-wise estimation. The method achieved a Root Mean Square Error (RMSE) of approximately 2.6 ppm, representing reductions of 49% and 18% compared to the considered empirical and numerical atmospheric models, respectively. Moreover, Dehvari et al. (2024) transformed ZWD values from an empirical model within the study region into B-spline coefficients and employed a data assimilation (DA) method to calibrate the estimated parameters at each epoch. Their results demonstrated a Root Mean Squared Error (RMSE) of approximately 0.8 centimeters for the ZWD estimations. The predicted ZWD values were then incorporated into the Single Point Positioning (SPP) method, resulting in an improvement of approximately 1.35 centimeters compared to the conventional approach using empirical ZWD values.

However, while they only employed the DA method for calibration, the Dynamic Mode Decomposition (DMD) method was used for predicting ZWD values, which necessitates 30 days of historical observations. In contrast, the C/DA method not only delivers highly accurate ZWD values during the analysis step (estimation of the current time) but also calibrates model parameters to enable more accurate short-term predictions. For instance, Kosary et al. 2022) applied the Ensemble Kalman Filter (EnKF) method (Evensen, 2003) to sequentially calibrate parameters of the International Reference Ionosphere (IRI) empirical model, improving short-term Total Electron Content (TEC) predictions. They utilized the predicted TEC values using C/DA method into an SPP experiment which the results showed a significant improvement in positioning accuracy.

This study proposes a C/DA approach to improve the estimation and prediction of Zenith Wet Delay (ZWD) values, which will be implemented as constraints in the PPP method. To achieve this, an empirical regional ZWD model (referred to as PCA-ZWD) was first constructed using Principal Component Analysis (PCA) to serve as the background model in the C/DA procedure. The model's parameters were then calibrated using the EnKF method, integrating ZWD values observed from approximately 309 GNSS stations across the central Europe into the model. The calibrated model parameters at each epoch have been used to estimate and predict ZWD values across the region of study. These values then applied as constraints in the PPP method (referred to as PPP-DA) at 10 GNSS test stations within the study area. The objective of this study is to

evaluate the effectiveness of the PPP-DA method in improving positioning accuracy and reducing convergence time, compared to traditional PPP approaches and PPP utilizing ZWD constraints from GFS model (PPP-GFS). The evaluation period spans the entire year of 2021, during which the C/DA method was applied to estimate the calibrated model parameters. Based on these estimates, the estimated ZWD values were then implemented into the PPP method. Preliminary results show an improvement of approximately 2 millimeters in positioning accuracy and a reduction in convergence time by about 6 minutes for the PPP-DA method compared to conventional PPP.

The subsequent sections begin with the construction of the proposed empirical model, followed by a concise explanation of the PPP-DA method. Next, the study region and the datasets used are described. This is followed by the presentation and discussion of the numerical results. Finally, the conclusion of this research is provided in the last section.

2. Data and materials

The study region for this research is located in central Europe, covering latitudes 44° to 55° and longitudes 5° to 15°. The proposed empirical model, PCA-ZWD, was developed specifically for this region. For data assimilation, ZWD values from 309 existing stations provided by the Nevada Geodetic Laboratory (NGL) were utilized (Blewitt et al., 2018). This facility archives extensive atmospheric delay information from global sources. Since the focus of this study is on assimilating ZWD values, archived observations from this data center were employed. For real-case scenarios, the PPP method can be applied to estimate ZWD values for any regional network, which can then be incorporated into the assimilation technique. The evaluation period for this study spanned from January 1 to December 31, 2021. During this period, the PCA-ZWD empirical model was evaluated by comparing its derived ZWD values against those from the GFS and Empirical Reanalysis Fifth generation (ERA5; Hersbach et al. 2020) numerical models, using ZWD values from 11 NGL stations that were not included in the C/DA method. Furthermore, to enhance the evaluation of both the proposed empirical model and the C/DA method, their derived ZWD values were compared with ZWD values derived from observations of 11 radiosonde stations. Radiosonde stations measure various atmospheric parameters, including temperature, pressure, and relative humidity at different pressure levels. These measurements are used to compute wet refractivity profiles across altitudes, which are then integrated to derive ZWD values (Forootan, Dehvari, et al., 2021). Due to their high vertical resolution and accuracy, radiosonde-derived ZWD values are widely regarded as a reliable external reference in atmospheric research for model evaluation (Dehvari et al., 2024a, 2024b; Forootan et al., 2023). Additionally, the proposed PPP method was evaluated using data from 10 IGS GNSS stations within the same timeframe. To further support the analysis, the GFS dataset for the evaluation period was utilized. By leveraging temperature and relative humidity data from various atmospheric layers provided by the GFS, we computed the ZWD values for the study region (Dehvari et al., 2024b). These computed ZWD values were subsequently incorporated as constraints in the PPP method (PPP-GFS).

Figure 1b shows the geographical location of the study region, while Figure 1a illustrates the spatial distribution of NGL stations (red circles), NGL test stations (magenta squares), radiosonde stations (yellow triangles), and IGS GNSS stations (blue hexagrams) within the study area.

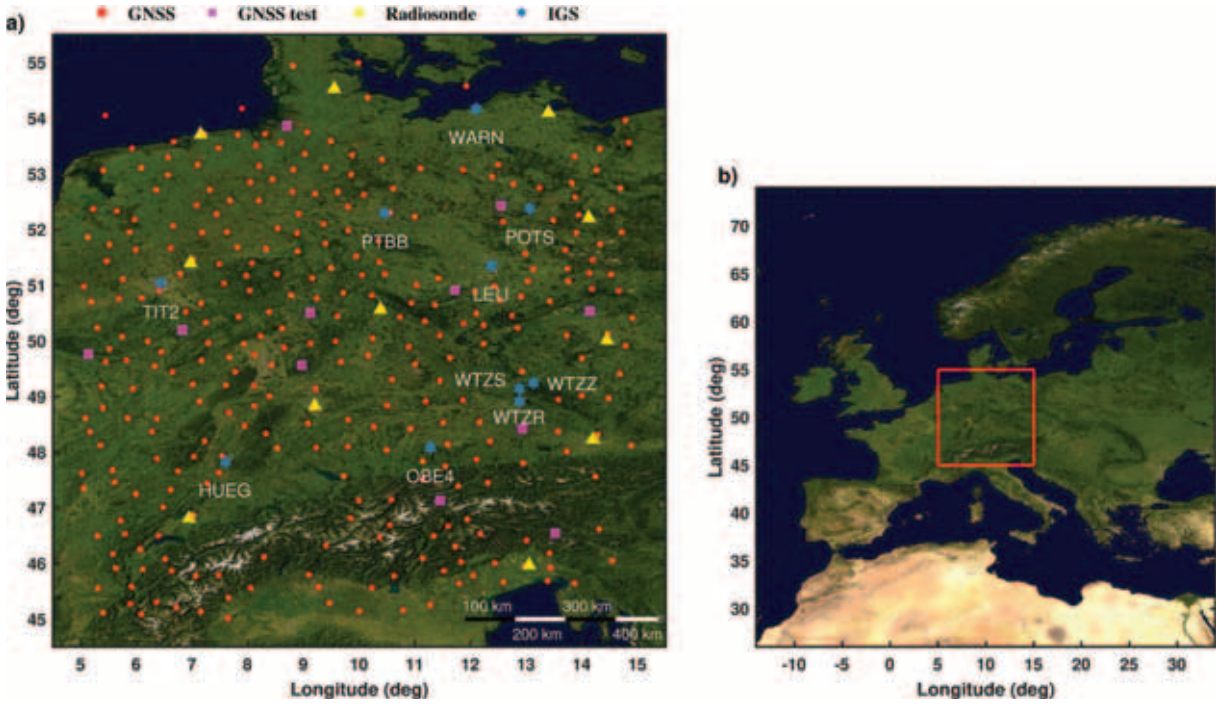

Figure 1. (a) Spatial distribution of observation stations used in this study, including NGL stations (red circles), NGL test stations (magenta squares), radiosonde stations (yellow triangles), and IGS GNSS stations (blue hexagrams). (b) Geographical location of the study region.

3. Methodology

3.1. Construction of the PCA-ZWD model

Empirical atmospheric models are constructed using numerical atmospheric models (e.g. ERA5 (Hersbach et al., 2020) or ERA-Interim (Dee et al., 2011)) and are capable of modeling the low-frequency variations of atmospheric delay parameters (Dehvari et al., 2023). These models are often represented as grid-based coefficients covering the globe (e.g., GPT3 (Landskron & Böhm, 2018) or GTrop (Sun et al., 2019) models or as a set of coefficients derived from a functional model (e.g., GZTD series (Yao et al., 2016) or IR-ZWD model (Dehvari et al., 2023)). Since we aim to use an empirical model within a data assimilation method, the corresponding parameters need to be represented as a unique set with a minimal number of coefficients, ensuring the model remains efficient and manageable for accurate assimilation. In grid-based models, each grid point has a unique set of coefficients for different atmospheric parameters. On the other hand, functional models aim to address this issue. However, in these models, different sets of coefficients are estimated for each frequency of the atmospheric delay parameter. Consequently, both types of models involve a relatively large number of coefficients. Ma et al. 2021 introduced a global atmospheric model based on Empirical Orthogonal Function (EOF) analysis, achieving an RMSE of approximately 3.65 cm for atmospheric delay values. While this model represents atmospheric delay with a single set of parameters, it has a spatial resolution of around 12 degrees, which may overlook local phenomena in regional networks.

In this study, we developed an empirical regional atmospheric wet delay model using dimensionality reduction techniques, specifically EOF and PCA. These techniques are known for their ability to capture the most significant patterns in data while minimizing noise and redundancy (I. T. Jolliffe & Cadima, 2016). For this purpose, we utilized ZWD values derived from ERA5 data at various altitudes within the study region. The construction of the empirical model involved organizing ZWD values from three consecutive years (2018, 2019, and 2020) into a 2-dimensional matrix (O_{ZWD}), where columns represent different locations and rows represent ZWD values over time. Subsequently, the covariance matrix (Q) of the ZWD values was computed as follows:

$$Q = \frac{1}{m-1} O_{ZWD}^T O_{ZWD} \tag{1}$$

where m is the number of observation epochs. By performing eigenvalue decomposition, the covariance matrix can be expressed as follows (I. Jolliffe, 2005):

$$Q = \mathrm{FVF} \tag{2}$$

Where F is an orthogonal matrix containing the eigenvectors of matrix Q, and V is a diagonal matrix containing the corresponding eigenvalues. The eigenvalues indicate the amount of variance captured by each principal component. It should be noted that F contains EOFs , which capture the spatial variations in the data. The temporal variations (PCs) are stored in S, which are computed by projecting O_{ZWD} onto the EOFs (F) as follows:

$$S = O_{ZWD}\mathrm{F} \tag{3}$$

The first columns of S and F indicate the most significant temporal (PCs) and spatial (EOFs) variations, respectively. Utilizing these primary principal components not only ensures the modeling of the main behavior of the data but also reduces noise and the number of parameters needed to reconstruct the dataset. Therefore, the ZWD values can be reconstructed using a reduced number of principal components (PCs) and EOFs as follows:

$$\hat{O}_{ZWD} = S_{k_n}\mathrm{F}_{k_n}^T \tag{4}$$

Where k_n is the number of the truncated principal components. Taking into account the eigenvalues stored in the V matrix, we set k_n to one in this study, as the first principal component captures approximately 98% of the total variation. As a result, the dimensions of the S_{k_n} and F_{k_n} matrices become $m \times 1$ and $n \times 1$, respectively, where m represents the number of epochs and n represents the number of points. To construct the ZWD model, B-spline functions (Schmidt et al., 2011) were fitted to both the spatial (F_{k_n}) and temporal (S_{k_n}) variations derived from PCA. Details for the implementation of B-spline functions can be found in (Forootan, Dehvari, et al., 2021; Limberger, 2015; Schmidt et al., 2011).

To construct the B-spline model based on PCA-derived values, it is first necessary to determine the optimal order of the B-spline functions. An empirical approach was employed for this purpose (Al-Fanek, 2013; Dehvari et al., 2023; Forootan, Farzaneh, et al., 2021). Specifically, models with varying B-spline orders were constructed to capture both spatial and temporal variations. The performance of each configuration was then evaluated by calculating the relative error between the modeled values and the original PCA-derived values. The combination of B-spline orders that resulted in the lowest relative error was selected as the optimal setup for model construction. It is important to note that different B-spline orders result in varying numbers of model coefficients, which influence both the model's complexity and its numerical conditioning.

This consideration, along with minimizing the relative error, was taken into account when selecting the best-performing B-spline model configuration. For the spatial domain, a 3D B-spline model was adopted. B-spline orders ranging from 2 to 4 were tested for the two horizontal directions, while orders 2 and 3 were considered for the vertical direction. Our investigation showed that increasing the B-spline order beyond 4 (horizontal) or 3 (vertical) caused ill-conditioning due to the excessive number of unknowns. For the temporal domain, a 1D B-spline function was used. B-spline orders from 2 to 5 were evaluated to model the temporal variation of the PCA values.

Figure *2* presents the relative error associated with each tested configuration, illustrating the results of the empirical optimization for both spatial and temporal modeling. In this figure, alongside the relative error for each configuration, the corresponding number of model coefficients is also presented.

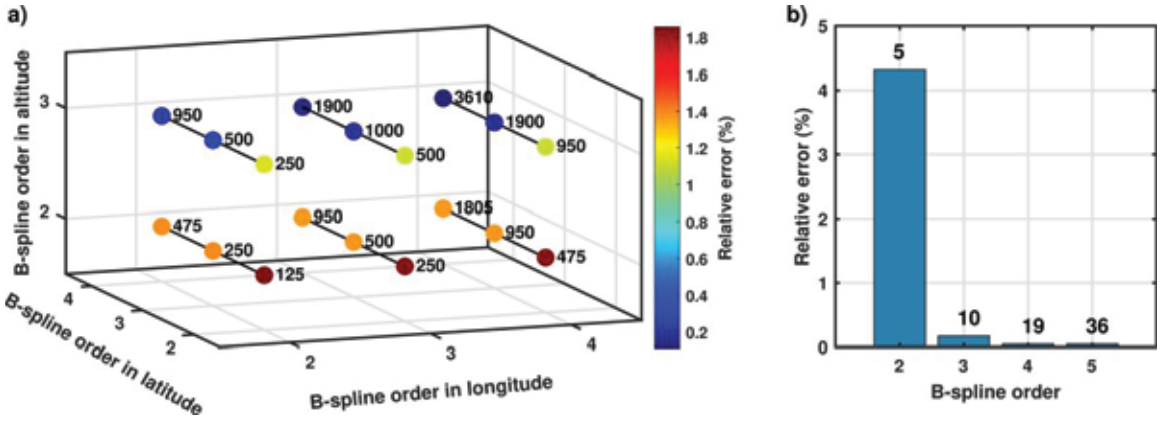

Figure 2. Calculated relative error for different sets of B-spline orders used in modeling spatial variations (a) and temporal variations (b). In this figure, the corresponding number of coefficients, resulting from the combination of different B-spline orders, is shown alongside each configuration.

From

Figure 2, it can be observed that increasing the order of the B-spline generally leads to a reduction in relative error. However, this improvement in accuracy comes at the cost of a higher number of model coefficients, which increases the model's complexity. Since the goal of this study is to develop an empirical model that achieves both low relative error and a manageable number of coefficients for C/DA method, a trade-off between these two factors must be considered. Based on this consideration and as shown in

Figure *2*a, we selected B-spline orders of 2, 3, and 3 for the longitude, latitude, and vertical directions, respectively, for modeling spatial variations. While other configurations yielded slightly lower relative errors, they resulted in significantly more coefficients. The chosen configuration provides a good balance, achieving a relative error close to the minimum while keeping the number of coefficients around 500. Similarly, for modeling temporal variations, a B-spline order of 3 was selected. This configuration also offers a reasonable balance between model simplicity and accuracy, requiring only 10 coefficients.

Consequently, the total number of coefficients in the proposed PCA-ZWD method is approximately 510, allowing for the calculation of ZWD values based on location and day of the year. Figure 3a illustrates the relative error between the derived spatial variations (EOF 1) and

those modeled using B-spline functions. Additionally, the right panel of this figure presents the comparison between the derived temporal variations (PCA1) and the corresponding values modeled using B-spline functions.

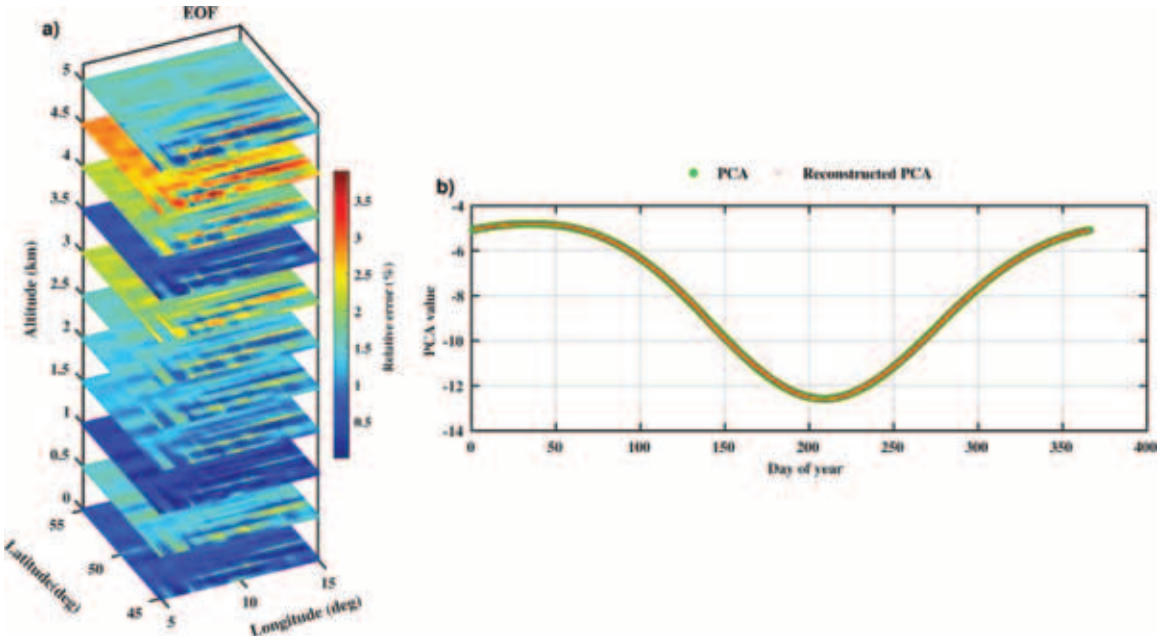

Figure 3. Relative error between the derived spatial variations (EOF 1) and those modeled using B-spline functions (a). The right panel (b) shows the comparison between the temporal variations derived from PCA 1 and the corresponding B-spline modeled values.

From Figure 3, it is evident that using B-spline functions effectively modeled the temporal (PCA 1) and spatial (EOF 1) variations. The maximum relative error in the spatial variations is approximately 3.8%, which occurs at altitudes around 4.5 km. This elevation is higher than the maximum elevation within the study region, and therefore, it will not affect the ZWD calculations performed at the Earth's surface using the proposed method. Additionally, since the PCA values capture the temporal variations of ZWD, the corresponding annual and semi-annual patterns are clearly visible in the right panel of this figure.

3.2. Calibration and Data Assimilation (C/DA) Method

The main challenge for empirical atmospheric models is their limited ability to capture spatial and temporal variations, leading to poor performance in modeling severe ZWD fluctuations (Dehvari et al., 2024a). To address this, we aimed to improve both the estimation (analysis phase) and short-term prediction of ZWD values by employing a C/DA approach. This approach integrates the provided observations and their associated uncertainties with those of the background model parameters, resulting in a calibrated set of parameters (state vector parameters) that improve accuracy in both estimation and prediction steps. The EnKF method (Evensen, 2003) is commonly used as the assimilation core in the C/DA approach due to its ability to effectively manage nonlinear dynamic systems, especially in atmospheric sciences (Forootan et al., 2024; Tang et al., 2022). In this approach, the state vector and its uncertainty are represented by a set of ensembles, making it well-suited for systems with nonlinear dynamics

(Houtekamer & Zhang, 2016). Considering the model parameters (w) as the state vector, the ensemble of state vector and observations is computed using the EnKF as follows:

$$W_f = w + \delta_j \quad (5)$$

$$M = m_t + \sigma_j \quad (6)$$

where m_t represents the observations at time t, and σ_j denotes the uncertainty associated with those observations. The index j ranges from 1 to k, where k is the number of ensembles. In this study, the ensemble size is set to 90, resulting in a state vector ensemble with dimensions of approximately 510×90. The ensemble size of 90 was selected based on prior DA and C/DA studies in atmospheric sciences (Dehvari et al., 2024a, 2024b; Forootan et al., 2024; Kosary et al., 2022). Although a formal sensitivity analysis was not conducted in this study, this ensemble size has been shown to provide stable and reliable performance in similar applications. δ_j represents random Gaussian noise associated with the state vector parameters, scaled to about 1% of each parameter (Kosary et al., 2022). Using these equations, the variance-covariance matrix of the state vector parameters (R_w) and the Kalman Gain (R_w) are calculated as:

$$R_w = \frac{(W_f - \bar{W}_f)(W_f - \bar{W}_f)^T}{k-1} \quad (7)$$

$$G_k = R_w A_t^T (R_m^T + A_t R_w A_t^T)^{-1} \quad (8)$$

Here, $\bar{W}_f$ represents the mean state vector parameters, R_m is the variance-covariance matrix of the observations, and $A_t$is the design matrix for observations based on the B-spline functions. At each epoch, the calibrated state vector parameters (W_e) and their mean value ($\bar{W}_e$) can be estimated as:

$$W_e = W_f + G_k(M - A_t W_f) \quad (9)$$

$$\bar{W}_e = \bar{W}_f + G_k(\bar{M} - A_t \bar{W}_f) \quad (10)$$

Using this approach, ZWD values at each epoch are assimilated into the background model, leading to calibrated state vector parameters. These calibrated parameters can then replace the original PCA-ZWD model's parameters to calculate ZWD values for the study region, either for the current state (analysis phase) or for forecasting purposes.

3.3. PPP-DA method

To mitigate the ionospheric effect, the ionospheric-free combination of dual-frequency observations is commonly employed. Using this combination, the linearized equations for the observed code and phase measurements can be expressed as follows (Subirana et al., 2013):

$$C_{IF}^s = \rho_r^s + T_r^s + dt_r - dt^s + b_{r.IF} - b_{IF}^s + \varepsilon_p \quad (11)$$

$$\varphi_{IF}^s = \rho_r^s + T_r^s + dt_r - dt^s + \lambda_{IF} N_{IF}^s + B_{r.IF} - B_{IF}^s + \varepsilon_\phi \quad (12)$$

Where C_{IF}^s and φ_{IF}^s are the ionospheric-free code and phase observations from satellite s to receiver r, respectively. ρ_r^s is the geometric range between the receiver and satellite, and T_r^s represents the tropospheric delay affecting the signal. dt_r and dt^s are the receiver and satellite clock biases, respectively. The parameters $b_{r.IF}$ and b_{IF}^s are the receiver and satellite hardware delays for the ionospheric-free code combination, respectively. Similarly, $B_{r.IF}$ and B_{IF}^s represent the receiver and satellite hardware delays for the ionospheric-free phase combination, respectively. λ_{IF} is the wavelength of the ionospheric-free combination of the carrier signal, and N_{IF}^s is the integer ambiguity for the ionospheric-free combination. Finally, ε_p and ε_ϕ are the

measurement noise for the code and phase observations, respectively. In these equations, the tropospheric delay (T_r^s) is separated into Zenith Hydrostatic Delay (ZHD) and Zenith Wet Delay (ZWD) components. The ZHD can be computed using established models (e.g. GPT3 model), while the ZWD is estimated as an unknown parameter. Consequently, the unknown parameters in these equations are the receiver position, ZWD value, and the integer ambiguity. In this study, we incorporate the ZWD values derived from the C/DA method as additional constraints in the system of equations used to estimate the unknown parameters. By doing so, the ZWD value at each epoch is added to the observation vector, and its associated uncertainty is integrated into the observation covariance matrix. Thus, at each epoch, the observation vector and the corresponding covariance matrix can be expressed as follows:

$$y_t = \begin{bmatrix} C_{IF}^s \\ \varphi_{IF}^s \\ ZWD_{C/DA} \end{bmatrix} \tag{13}$$

$$Q_t = \begin{bmatrix} \sigma_{C_{IF}}^2 & 0 & 0 \\ 0 & \sigma_{\varphi_{IF}}^2 & 0 \\ 0 & 0 & \sigma_{ZWD_{C/DA}}^2 \end{bmatrix} \tag{14}$$

Where $\sigma_{C_{IF}}^2$ and $\sigma_{\varphi_{IF}}^2$ represent the variances for the ionospheric-free combination code and phase measurements, respectively. Additionally, $\sigma_{ZWD_{C/DA}}^2$ denotes the variance associated with the ZWD values derived from the C/DA method. Using this approach, we aimed to evaluate the performance of the PPP method when incorporating ZWD values from the C\DA method as constraints.

To implement the static PPP method, the following processing strategies were employed: The ionosphere-free linear combination was used to eliminate ionospheric delay effects, while observation uncertainties were assigned as 0.3 m for GNSS pseudo range measurements and 0.003 m for carrier phase observations (Gong et al., 2024). Additionally, the uncertainties assigned to the ZWD values from the C/DA and GFS models were set to 1.0 cm and 1.5 cm, respectively. These values were chosen based on the comparative evaluation of both models against GNSS and radiosonde observations, where the C/DA method demonstrated better performance. A detailed analysis is provided in Section 4.1 and Figure 5. It should be noted that these values were not applied as fixed constraints but were incorporated into the PPP formulation as uncertainty terms (representing the uncertainty of ZWD values in equation (14)), ensuring a realistic weighting scheme. Meanwhile, the direct ZWD values from each method were used as prior values (as presented in equation (13)).

An elevation-dependent weighting scheme determined the observation weights, with a cut-off elevation angle set to 15°. Tropospheric hydrostatic delay (ZHD) corrections were calculated using the GPT3 model (Landskron & Böhm, 2018). This model is a widely used empirical atmospheric model, commonly applied in precise GNSS positioning applications (Glaner & Weber, 2023; Herring et al., 2010). The ZHD estimates derived from GPT3 are typically more accurate than its corresponding ZWD estimates. The reported root mean square (RMS) error for ZHD values is approximately 1.1 cm, although this error may increase with geographical latitude (J. Li et al., 2022). In this study, the primary objective was to assess the impact of ZWD values derived from the C/DA method on PPP performance. For this purpose, the final precise orbit and clock products from IGS were used across all PPP solutions to ensure consistency. While these products are not suitable for real-time applications due to their latency, they offer high accuracy

for comparative analysis. It is acknowledged that using real-time orbit and clock products (e.g., from CNES or JAXA) might reduce the overall positioning accuracy; however, this effect would be consistent across all methods. Therefore, the observed differences in positioning results can still be attributed primarily to the influence of the assimilated ZWD constraints.
The reference coordinates for PPP evaluation were obtained from IGS daily station position files. Finally, the unknown parameters at each epoch were estimated using the Kalman filter algorithm. The same settings were consistently applied across all the PPP methods used in this study.

To assess the significance of the positional improvements achieved by the PPP-DA method, a 3D error ellipsoid representation was generated for each station at each epoch in the ENU (East-North-Up) coordinate system (For example see Figure 14). This approach provides a clear visual and quantitative means of comparing the uncertainty in the derived 3D positions. The covariance matrix of the position errors in the XYZ coordinate system was first transformed into the ENU frame using a rotation matrix based on the station's geographic location (Hofmann-Wellenhof et al., 2007; Leick, 2015). Eigenvalue decomposition of the ENU covariance matrix was then performed to obtain the ellipsoid's principal axes, which represent the positional uncertainty in the East, North, and Up directions. The lengths of these axes were determined by the square roots of the eigenvalues, while the corresponding eigenvectors provided the orientation of the ellipsoid in the ENU space. The ellipsoid was centered at the station's ENU position, and its surface was plotted to visualize the spatial extent of the positioning errors. If the ellipsoids from the two methods (e.g. conventional PPP and PPP-DA) do not overlap significantly (or not at all), this visually confirms that the improvement is statistically significant.

3.4. Evaluation parameters

To evaluate the ZWD values from various sources in this study, we utilized statistical metrics including Root Mean Squared Error (RMSE), Bias, and Correlation Coefficient (CC). These parameters are defined and calculated as follows (Dehvari et al., 2024b):

- **Root Mean Squared Error (RMSE)**: Represents the overall magnitude of errors between predicted and observed values. It is sensitive to large errors due to squaring the differences. A lower RMSE indicates better model accuracy.
- **Bias**: Represents the systematic error, defined as the difference between the mean of predicted and observed values. A positive bias indicates overestimation, while a negative bias indicates underestimation. A bias close to zero suggests minimal systematic error.
- **Correlation Coefficient (CC)**: Measures how well the predicted values follow the variations in observed values. A CC value close to 1 indicates a strong agreement in trends and fluctuations, meaning the model effectively captures atmospheric variations rather than excessively smoothing them.

$$RMSE = \sqrt{\frac{\sum_{i=1}^{n}(ZWD_m^i - ZWD_o^i)^2}{n}} \quad (15)$$

$$Bias = \frac{1}{n}\sum_{i=1}^{n} ZWD_m^i - ZWD_o^i \quad (16)$$

$$CC = \frac{1}{n-1}\sum_{i=1}^{n}(\frac{ZWD_m^i - \overline{ZWD_m}}{s_{ZWD_m}})(\frac{ZWD_o^i - \overline{ZWD_o}}{s_{ZWD_o}}) \quad (17)$$

where:

- ZWD_m^i: Modeled Zenith Wet Delay at $i-th$ sample
- ZWD_o^i: Observed Zenith Wet Delay at $i-th$ sample
- $\overline{ZWD_m}$: Mean of modeled ZWD
- $\overline{ZWD_o}$: Mean of observed ZWD
- s_{ZWD_m}: Standard deviation of modeled ZWD
- s_{ZWD_o}: Standard deviation of observed ZWD
- n: Total number of samples

For positioning accuracy evaluation, we first transformed the station coordinates, both from the IGS file and those derived from each PPP method, into the ENU (East, North, Up) coordinate system (Hofmann-Wellenhof et al., 2007). Using these transformed coordinates, we calculated the east (E_{error}), north (N_{error}), up (U_{error}), horizontal (H_{error}), and 3D position errors ($3D_{error}$) based on the following equations:

$$E_{error} = |E_{IGS} - E_{PPP}| \quad (18)$$
$$N_{error} = |N_{IGS} - N_{PPP}| \quad (19)$$
$$U_{error} = |U_{IGS} - U_{PPP}| \quad (20)$$
$$H_{error} = \sqrt{E_{error}^2 + N_{error}^2} \quad (21)$$
$$3D_{error} = \sqrt{E_{error}^2 + N_{error}^2 + U_{error}^2} \quad (22)$$

Where E_{PPP}, N_{PPP}, U_{PPP} are the East, North, and Up coordinates derived from the PPP method. Additionally, E_{IGS}, N_{IGS}, U_{IGS} are the East, North, and Up coordinates from the IGS reference file. It should be noted that the U_{error} is also commonly referred to as the vertical error.

4. Results and discussion

In this section, we start by evaluating the performance of the proposed C/DA method in predicting ZWD values at 11 selected GNSS test stations and 11 radiosonde stations. Finally, we assess the performance of the PPP method when constrained by the estimated ZWD values from the C/DA method (PPP-DA method).

4.1. Evaluation of the C/DA method

In this section, we compare the ZWD values obtained from the proposed C/DA method, GTrop, PCA-ZWD, GFS, and ERA5 models with the observed values from 11 GNSS test stations (indicated by magenta squares in Figure 1a) and the corresponding ZWD values derived from 11 radiosonde stations (indicated by yellow triangles in Figure 1a) within the study region. At each epoch, the available GNSS-derived ZWD values are integrated into the PCA-ZWD model through equation (5) to equation (10) to calibrate the background model parameters. Subsequently, using these calibrated parameters, the ZWD values for the GNSS test stations and radiosonde stations are calculated at the corresponding epochs, known as the analysis step. The estimated ZWD values from the analysis step are then evaluated against those from other models. The evaluation period spans from January 1 to December 31of the year 2021.

In comparison with GNSS test stations, Given the 6-hour temporal resolution of the GFS model, all comparisons are conducted at this same temporal resolution. Figure 4 presents the calculated RMSE (a, b, c, and d), Bias (e, f, g, and h), and CC (i, j, k, and l) values from the comparison across each of the test stations. Additionally, Figure 5 shows a heat map table displaying the mean statistical parameters for each model, serving as a summary of the evaluation results. In this figure, the performance of each model is illustrated using a color-coded scheme, where the bluest cell in each column represents the best-performing model, while the worst-performing model is indicated by a white-colored cell.

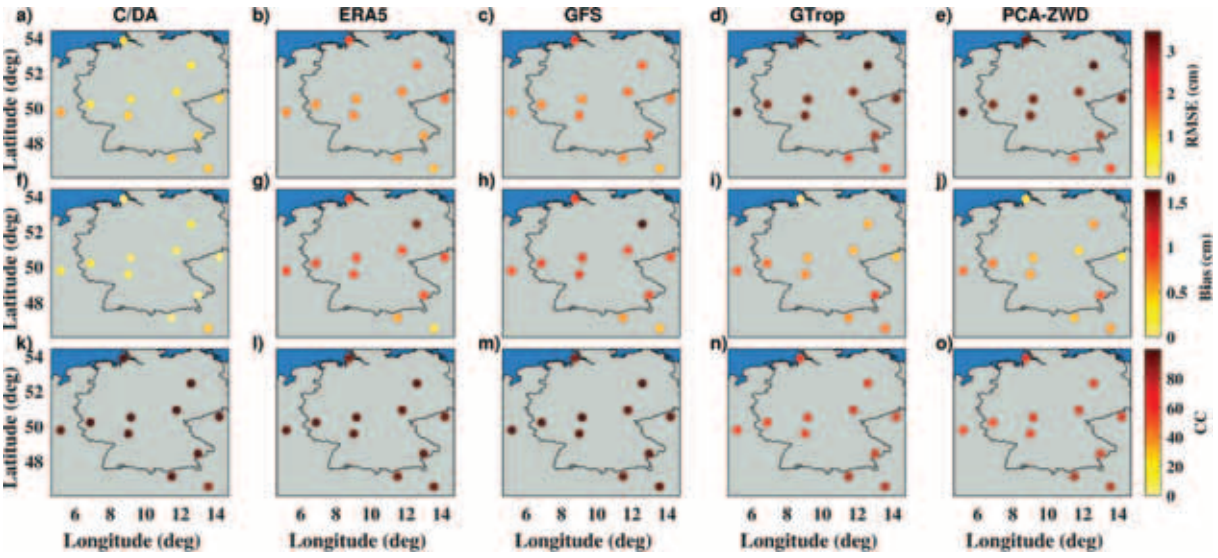

Figure 4. Calculated RMSE (a, b, c, and d), Bias (e, f, g, and h), and CC (i, j, k, and l) for the analysis step from the comparison of ZWD values from GNSS test stations with the corresponding values from the C\DA method, ERA5, GFS, GTrop, and PCA-ZWD models for the entire year of 2021.

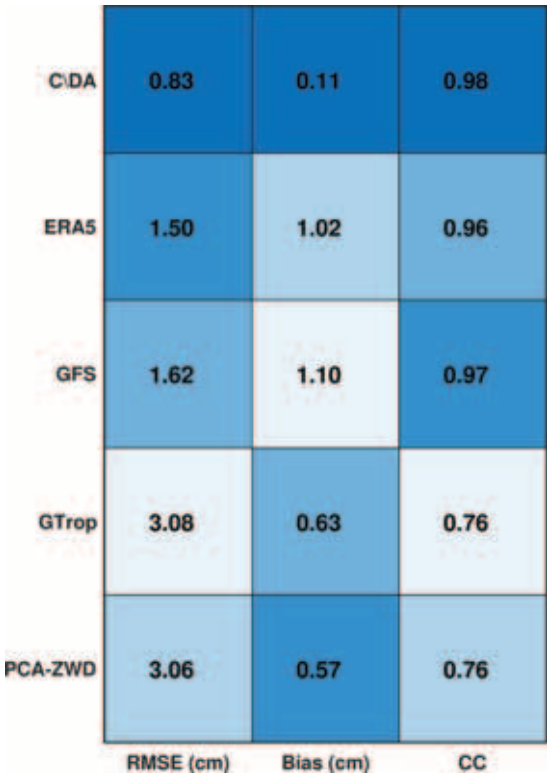

Figure 5. Calculated mean statistical parameters for the analysis step from the comparison of ZWD values derived from the C\DA method, ERA5, GFS, GTrop, and PCA-ZWD models with corresponding GNSS test station observations for the entire year of 2021.

Figure 5 clearly illustrates that the C\DA method significantly outperforms the ERA5, GFS, GTrop, and PCA-ZWD models during the analysis step, particularly in terms of RMSE, Bias, and CC values. Specifically, the RMSE for the C\DA method is reduced by 44%, 48%, 73%, and 72% compared to the ERA5, GFS, GTrop, and PCA-ZWD models, respectively. Furthermore, the C/DA method shows an improvement in CC values, achieving increases of 1% over the ERA5 model, 2% over the GFS model, and 22% over both the GTrop and PCA-ZWD models. Additionally, the Bias is notably lower by approximately 88%, 89%, 82%, and 80% when compared to those same models, showcasing its enhanced accuracy and reliability. From Figure 5, it is evident that the two considered numerical models (ERA5 and GFS) outperform the two empirical models in terms of RMSE and CC values. However, the Bias values for the GFS and ERA5 models, approximately 1.1 cm and 1.0 cm respectively, are higher than those observed for the empirical models. This indicates that, although the numerical models more accurately capture the overall variability (as reflected by lower RMSE and higher CC values), they tend to systematically underestimate the ZWD values, leading to a higher positive bias.

For further investigation, similar to the comparison with the GNSS test stations, the ZWD values derived from the C/DA method, PCA-ZWD, GTrop, ERA5, and GFS models were compared with the corresponding ZWD values calculated from the observations of the 11 radiosonde stations. The comparison covers the entire year of 2021. Given that radiosonde observations have

505 a temporal resolution of approximately 12 hours, the comparison was performed at a 12-hour
506 temporal resolution. Figure 6 displays the calculated RMSE, Bias, and CC values for each
507 radiosonde station. Meanwhile, Figure 7 provides a heat map that summarizes the mean
508 statistical parameters for each model.

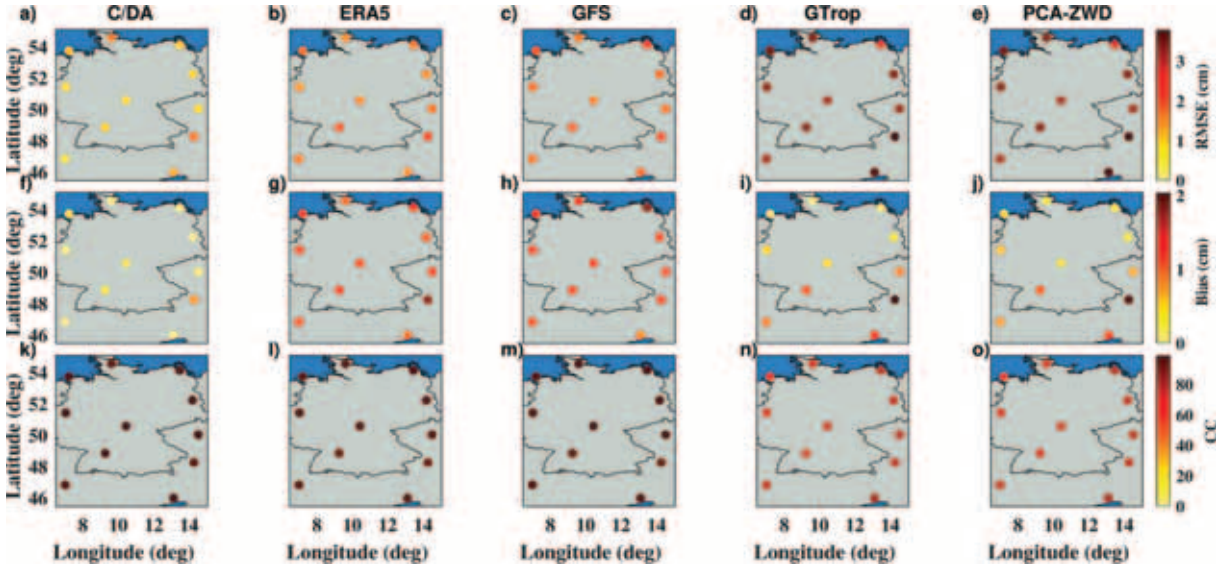

Figure 6. Calculated RMSE (a, b, c, and d), Bias (e, f, g, and h), and CC (i, j, k, and l) values from the comparison of ZWD values obtained from radiosonde stations with those derived from the C/DA method, ERA5, GFS, GTrop, and PCA-ZWD models for the entire year of 2021.

509

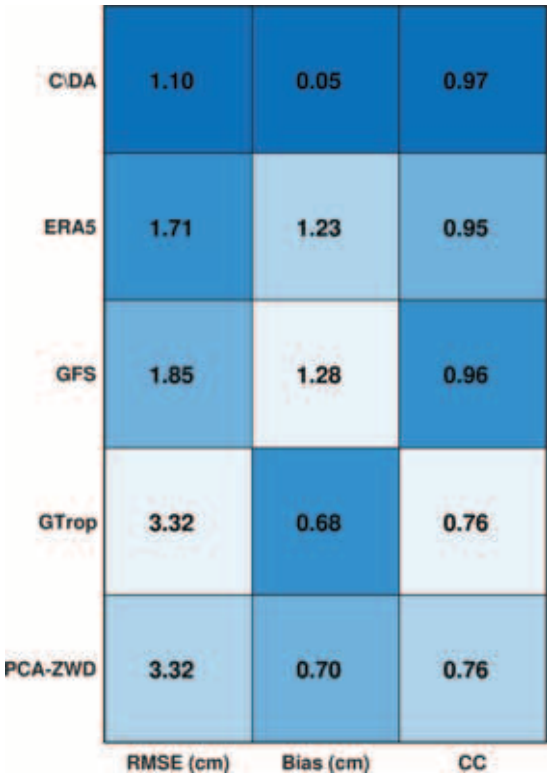

Figure 7. Mean statistical parameters (RMSE, Bias, and CC) from the analysis step, comparing ZWD values derived from the C/DA method, ERA5, GFS, GTrop, and PCA-ZWD models with corresponding observations from radiosonde stations throughout the year 2021.

510

511 As illustrated in Figure 7 and consistent with the findings from the GNSS test station
512 comparison, the C/DA method demonstrates a clear advantage over the ERA5, GFS, GTrop, and
513 PCA-ZWD models during the analysis step. The C/DA method reduces the RMSE by 35%, 40%,
514 67%, and 66% compared to GFS, GTrop, and PCA-ZWD, respectively. It also shows an
515 improvement in correlation, with CC values increasing by 3% relative to ERA5, 2% relative to
516 GFS and by 21% compared to both GTrop and PCA-ZWD. Moreover, the Bias associated with
517 the C/DA method is substantially lower by approximately 96%, 96%, 94%, and 93% when
518 compared to the ERA5, GFS, GTrop, and PCA-ZWD models, further highlighting its enhanced
519 accuracy and robustness. Overall, these results confirm that, even when evaluated against an
520 independent external data source (radiosonde stations), the C/DA method consistently
521 outperforms the considered numerical and empirical atmospheric models during the analysis
522 step.

523 Comparing the proposed PCA-ZWD model with the widely recognized GTrop model (Sun et al.,
524 2019), it is observed that the PCA-ZWD model demonstrates a slight performance improvement.
525 Specifically, the RMSE and Bias values of the PCA-ZWD model are approximately 5% and
526 9.5% lower than those of the GTrop model, respectively, indicating its advantage in regional
527 atmospheric modeling. Moreover, considering the region of study and the 1-degree spatial
528 resolution of the GTrop model (Sun et al., 2019), it requires approximately 726 location-

dependent coefficients to model ZWD values. This location-specific nature limits its compatibility with the C\DA method. In contrast, the proposed PCA-ZWD model uses only about 510 parameters, which are designed to calculate ZWD values at any location within the study area, making it more efficient and better suited for C\DA implementation.

The calibrated PCA-ZWD coefficients obtained through the C/DA method can also be used to predict ZWD values for future epochs (prediction step). To evaluate this prediction capability, the calibrated background model parameters from each epoch throughout 2021 were used to forecast ZWD values up to 24 hours ahead, with a temporal resolution of 1 hour. The predicted ZWD values, along with those from the GTrop, GFS, ERA5, and PCA-ZWD models, were compared with corresponding observations from 11 GNSS test stations and 11 radiosonde stations within the study region. Figure 8 show the calculated RMSE (a), Bias (b), and CC (c) values for each prediction time step derived from the comparison with GNSS test stations. In this figure, the statistical parameters for the C/DA predicted ZWD values, ERA5, GFS, GTrop, and PCA-ZWD models are represented by red, magenta, blue, green, and brown lines, respectively. Moreover, the results of the prediction step comparison with the radiosonde stations are presented in Figure 9.

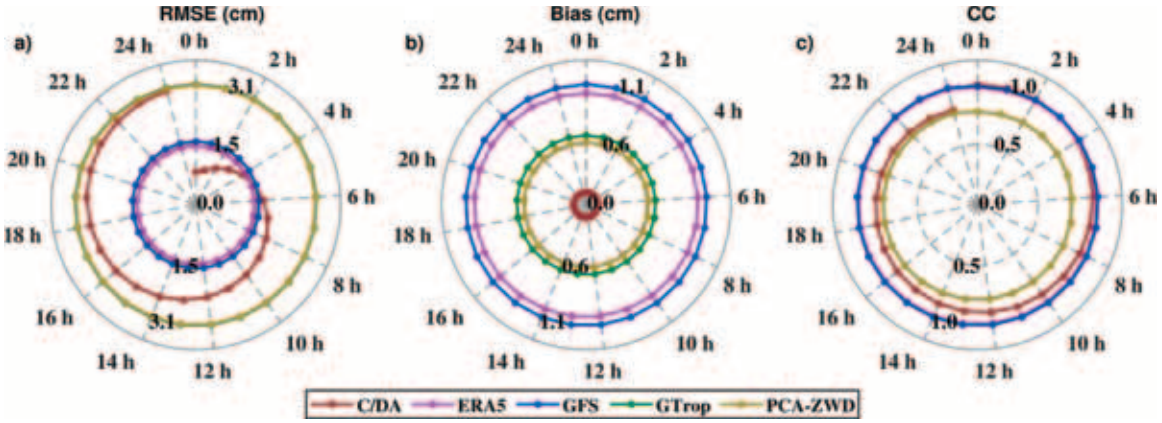

Figure 8. Calculated RMSE (a), Bias (b), and CC (c) for the prediction step, comparing ZWD values from GNSS test stations with those from the C/DA method (red line), ERA5 (magenta line), GFS (blue line), GTrop (green line), and PCA-ZWD (brown line) models throughout 2021 across various prediction time steps.

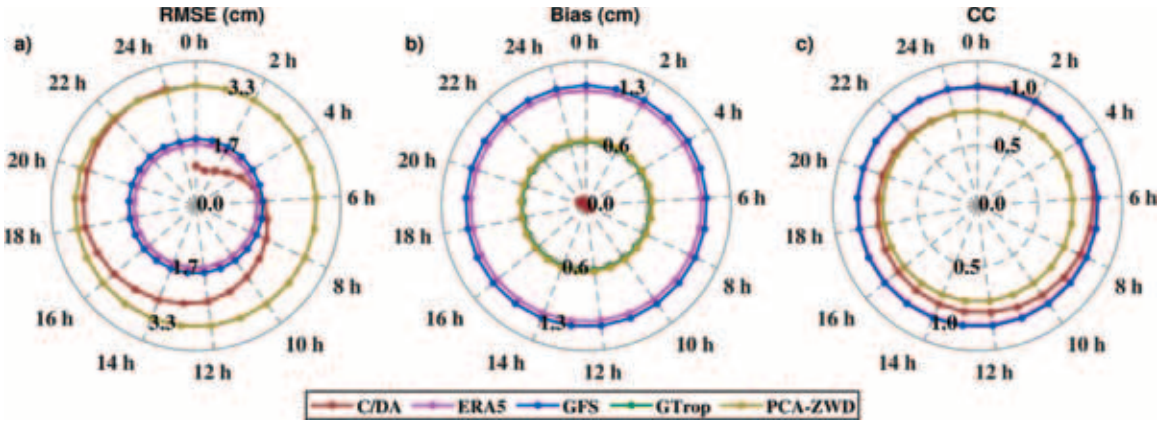

Figure 9. RMSE (a), Bias (b), and CC (c) calculated for the prediction step by comparing ZWD values from radiosonde stations with those predicted by the C/DA method (red line), ERA5 (magenta line), GFS (blue line), GTrop (green line), and PCA-ZWD (brown line) models across different forecast lead times throughout 2021.

Referring to Figure 8, in comparison with GNSS test stations, the RMSE for the predicted ZWD values gradually increases with the extension of the prediction time span, at a rate of approximately 0.02 centimeters per hour. However, compared to the RMSE values from other models, it is evident that the C/DA method yields lower RMSE values than the ERA5 and GFS models for predictions up to 5 hours and remains lower than the two empirical models for prediction time spans up to 24 hours. Moreover, when comparing CC values, the decrease rate for the C/DA method is approximately 0.05 per hour. Despite this decline, the C/DA method maintains higher CC values than the ERA5 and GFS models for nearly 5 hours and demonstrates superior performance compared to the empirical models for prediction time spans of up to 24 hours. However, as shown in Figure 8, the Bias values of the C/DA method remain relatively stable across all prediction time spans up to 24 hours and are consistently lower than those of the other models. This consistent performance indicates that the C/DA method effectively minimizes systematic errors over the entire prediction period, outperforming the other models in maintaining low bias and reducing systematic deviations.

For the prediction step evaluated against radiosonde station observations, Figure 9 illustrates that the ZWD values predicted by the C/DA method achieve lower RMSE compared to the EA5 and GFS models for lead times up to 6 hours, and outperform the GTrop and PCA-ZWD models up to 24 hours. Similar to the results from the GNSS test station comparison, the C/DA method consistently yields lower Bias values than the other numerical and empirical models across all forecast intervals. In terms of correlation, the C/DA method shows slightly better CC values than the ERA5 and GFS models up to 6 hours and maintains superior performance compared to the empirical models (GTrop and PCA-ZWD) throughout the 24-hour prediction period.

Subsequently, the required processing times for the C/DA method, GTrop, and PCA-ZWD models were compared. It is assumed that the ZWD values from the reference stations (i.e., the GNSS stations used in this study) are readily available, and thus, only the processing time for executing the C/DA method itself has been evaluated. The GFS model was excluded from this evaluation due to its nature as a comprehensive numerical weather prediction model, which inherently involves significantly more complex and resource-intensive computations. This

analysis was conducted for the entire year of 2021, using the same observations employed in the C/DA method. Figure 10 displays the results of this comparison, with the processing times for the C/DA method, GTrop, and PCA-ZWD models represented by red, green, and brown lines, respectively. It should be noted that the processing times in this figure are shown on a logarithmic scale for better visualization.

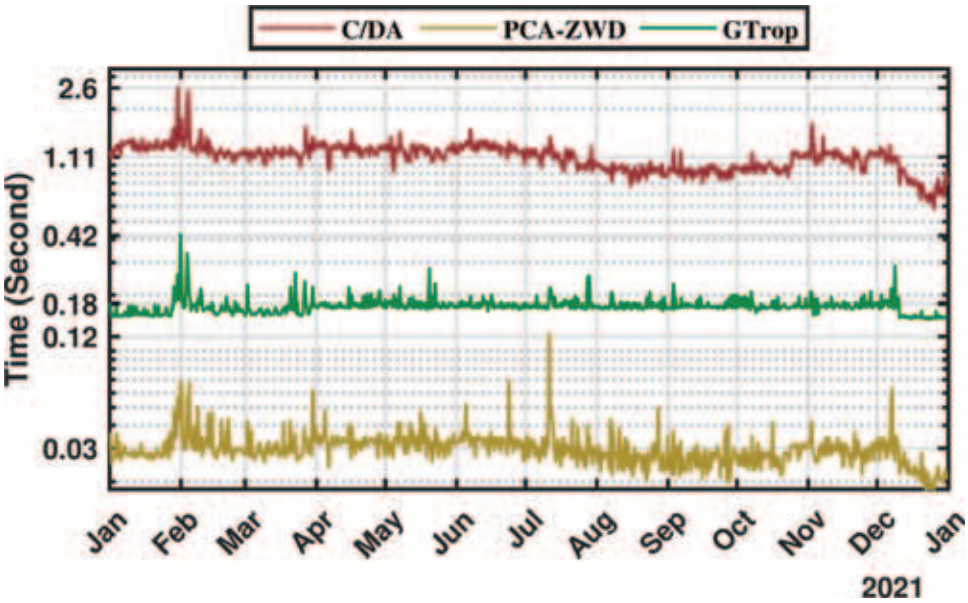

Figure 10. Calculated processing times for the C/DA method (red line), GTrop (green line), and PCA-ZWD models (brown line) over the entire year 2021.

Referring to Figure 10, it is evident that the C/DA method requires the highest computational cost and processing time among the evaluated models. However, the mean processing time for the C/DA method is approximately 1.1 seconds. Given the typical GNSS observation interval of 30 seconds, this processing time does not pose a limitation for potential real-time applications. When comparing the two empirical models, the PCA-ZWD model exhibits a lower mean processing time of 0.03 seconds, compared to 0.17 seconds for the GTrop model. This improvement is primarily due to the PCA-ZWD model's simpler structure and fewer required coefficients.

While the proposed C/DA method demonstrates promising results in enhancing the accuracy of ZWD prediction, certain limitations must be acknowledged. One key factor affecting the reliability of the method is the spatial distribution and density of reference GNSS stations within the region of study. A sparse or unevenly distributed network can limit the model's ability to accurately capture localized variations in tropospheric water vapor. This constraint may reduce the accuracy of the ZWD values derived during both the assimilation and prediction stages, particularly in areas with complex terrain or rapidly changing meteorological conditions. Additionally, the effectiveness of the C/DA approach in real-time applications depends on the timely acquisition and processing of ZWD data from reference stations. Any delays or gaps in the availability of reference data can impact the model's performance, especially for real-time or

near real-time positioning applications. These factors highlight the importance of a well-maintained GNSS infrastructure and suggest that future improvements in the spatial coverage and real-time accessibility of reference station data could further enhance the performance of the C/DA method.

In the next section, we will incorporate the ZWD values provided by the C/DA method into the PPP method to evaluate the impact of these values on its overall performance.

4.2. Evaluation of PPP-DA method

In this section, the ZWD values derived from the C/DA method and the GFS model were used as constraints in the Precise Point Positioning (PPP) method. The results were then compared to those obtained from the conventional PPP method, focusing on 3D positioning accuracy and convergence time. To evaluate the performance of the proposed PPP-DA method, we applied it to 10 selected GNSS stations (as shown in Figure 1a) for the year 2021. The one-year evaluation using 10 well-distributed IGS stations enables a robust assessment of the proposed method across diverse atmospheric conditions, including seasonal variations. Despite the limited number of stations, the extended time span ensures reliable conclusions. The results confirm that the improved ZWD estimation via the C/DA method leads to enhanced vertical positioning accuracy in PPP. The following sections present a detailed comparison of the positioning error and convergence time results.

4.2.1. Positioning error comparison

After applying the constraints to the PPP method using the ZWD values derived from the C/DA method (PPP-DA) and GFS model (PPP-GFS), the estimated positions for each station at each epoch were compared with the reference positions provided by the IGS service. Figure 11 illustrates the mean positioning error calculated in the east (a), north (b), up (c), and 3D directions (d) for each station throughout 2021. In this figure, the positioning errors for the conventional PPP, PPP-DA, and PPP-GFS methods are represented by green, red, and blue bars, respectively.

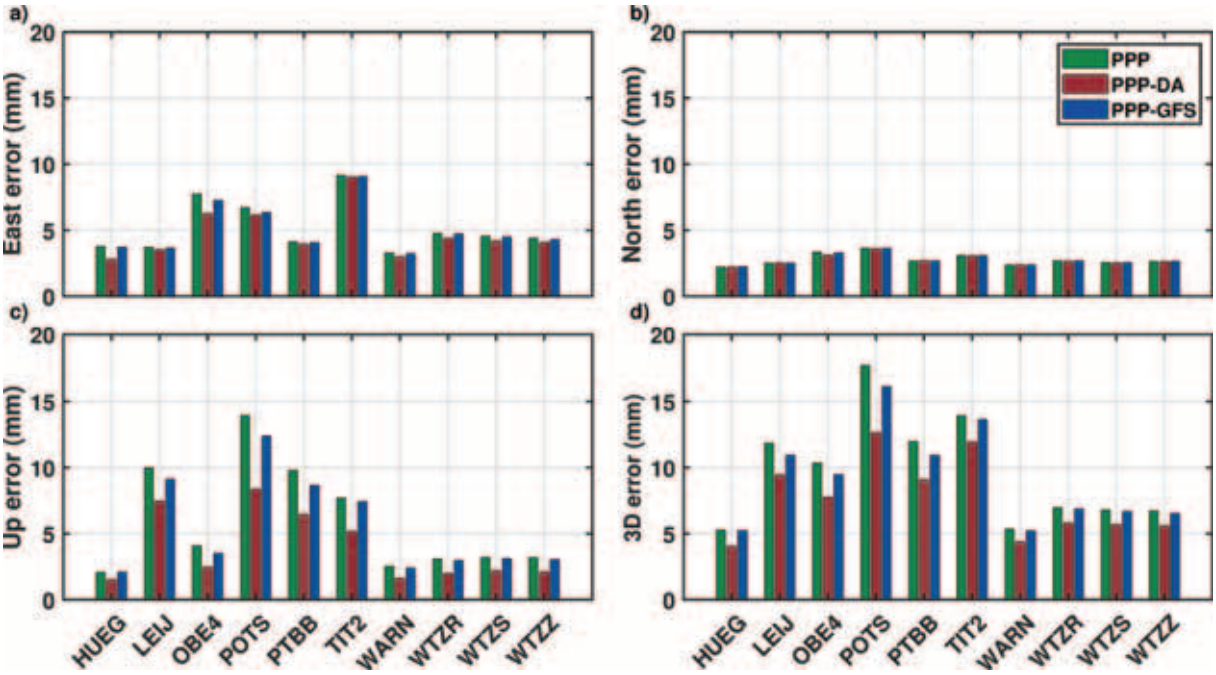

Figure 11. The calculated positioning errors in the east (a), north (b), up (c), and 3D (d) directions for each station. The green, red, and blue bars represent the positioning errors for the conventional PPP, PPP-DA, and PPP-GFS methods, respectively.

As shown in Figure 11, the positioning errors in the east, north, up, and 3D directions for the PPP-DA method are lower than those of the conventional PPP and PPP-GFS methods across all considered stations. In the east direction, the PPP-DA method achieves a mean positioning error of approximately 4.70 millimeters, representing an improvement of about 0.52 millimeters over the 5.22 millimeters from PPP and 0.3 millimeters over the 5 millimeters from PPP-GFS. In the north direction, the PPP-DA, PPP-GFS, and conventional PPP methods show positioning errors of approximately 2.76, 2.76, and 2.76 millimeters, respectively, indicating nearly identical performance across the models. In the up direction, the positioning errors for the PPP and PPP-GFS methods are approximately 5.95 and 5.45 millimeters, respectively. In contrast, the PPP-DA method shows an error of about 3.92 millimeters, representing an improvement of 2 millimeters over PPP and 1.55 millimeter over PPP-GFS. When comparing the positioning errors in the east, north, and up directions, it is clear that the PPP-DA method shows the greatest improvement in the vertical direction compared to the conventional PPP method. This result is expected as tropospheric delay has a more significant impact on vertical positioning accuracy. The introduction of high-accuracy ZWD values notably enhances positioning accuracy in this direction. For the 3D positioning error, the mean values for the PPP-DA, PPP, and PPP-GFS methods are approximately 7.6, 9.6, and 9.15 millimeters, respectively. This indicates that the PPP-DA method offers an improvement of about 2 millimeters over PPP (about 21% improvement) and 1.5 millimeters over PPP-GFS (about 16% improvement). Overall, it can be concluded that the PPP-DA method outperforms the other two methods in terms of positioning accuracy. Additionally, the PPP-GFS method demonstrates better performance than the conventional PPP method, indicating that incorporating ZWD values from the GFS model as a constraint can enhance the accuracy of the conventional PPP approach. Referring to the vertical errors presented in Figure 11, stations with higher vertical positioning errors under the

conventional PPP method show greater improvement when using the PPP-DA method. For example, at the POTS station, which had the highest vertical positioning error under the PPP method, the error was approximately 14 millimeters. The PPP-DA method reduced this to around 8.3 millimeters, resulting in an improvement of about 40% in accuracy.

From Figure 11, it is evident that the vertical positioning error is relatively large for some stations (e.g., POTS station). This vertical error is influenced by factors such as tropospheric delay, satellite geometry, and multipath effects. To investigate the relationship between vertical positioning error and ZWD values, we calculated the standard deviation of ZWD values derived from the PPP, PPP-DA, and PPP-GFS methods for each station over the evaluation period. Figure 12 presents these values, where the standard deviations for the PPP, PPP-DA, and PPP-GFS models are represented by green, red, and blue lines, respectively.

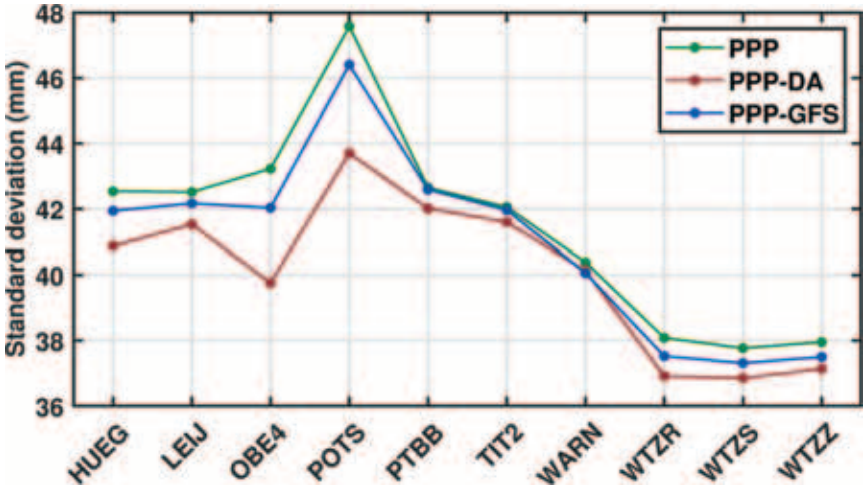

Figure 12. Standard deviation of ZWD values derived from the PPP (green line), PPP-DA (red line), and PPP-GFS (blue line) methods for the 10 selected stations throughout the entire year 2021.

By comparing the vertical positioning error in Figure 11 with the standard deviations in Figure 12, it is clear that the vertical positioning error for each station is closely related to the corresponding standard deviation of the introduced ZWD values. For example, the POTS station shows a larger standard deviation of ZWD values derived from the PPP method, which corresponds with the larger vertical error observed in Figure 11 for this station under the conventional PPP method. The standard deviations shown in Figure 12 represent the internal consistency of ZWD values from different sources and are indicative of their relative precision. Among all methods, the C/DA approach exhibits the lowest standard deviation, reflecting the highest precision. Additionally, as presented in Section 4.1, the C/DA-derived ZWD values demonstrate the lowest RMSE and highest correlation coefficient (CC) when compared to the reference datasets, confirming both their accuracy and consistency. Since vertical positioning error is strongly influenced by the accuracy of the applied ZWD constraints, the combination of high precision and high accuracy offered by the C/DA method leads to its superior performance in reducing vertical errors. Additionally, the ZWD values derived from the GFS model show a lower standard deviation compared to those from the PPP method. This reduction in variability corresponds with the improved positioning accuracy observed with the PPP-GFS method, which exhibits lower positioning errors compared to the conventional PPP method.

To assess the performance of each method over different time periods, we compared the positioning accuracy of the PPP, PPP-DA, and PPP-GFS methods across different months. For this analysis, during the evaluation period (the entire year 2021), the positioning accuracy from all 10 stations was separated by month to evaluate the accuracy for each distinct time period. Figure 13 illustrates the mean 3D positioning error for all considered stations, comparing the PPP (green line), PPP-DA (red line), and PPP-GFS (blue line) methods across different months.

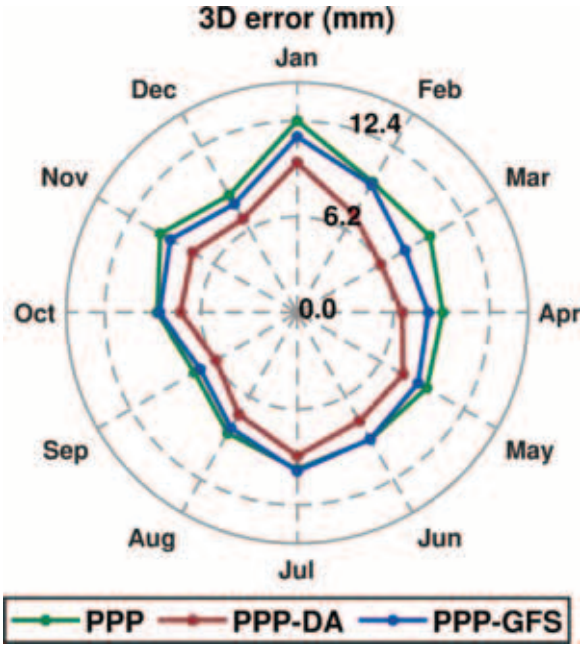

Figure 13. Mean 3D positioning error for each month, derived from all considered stations over the entire year of 2021. The corresponding values for the PPP, PPP-DA, and PPP-GFS methods are represented by green, red, and blue lines, respectively.

According to Figure 13, the proposed PPP-DA method has consecutively lower mean 3D positioning error over all months compared to the conventional PPP and PPP-GFS methods, which again indicate the superior performance of this method. Moreover, similar to the previous evaluation, the PPP-GFS method is also shows better performance than conventional PPP method.

To assess the significance of positioning improvement using the proposed PPP-DA method at each epoch, we used ellipsoidal error representation. For this aim at each epoch, the estimated station's position and corresponding uncertainty was first transformed to the ENU coordinate system. Afterward, the ellipsoidal error for each method has been calculated, centered at stations derived ENU position. For example, Figure 14 illustrates the ellipsoidal error representation for the HUEG station on January 1, 2021. The magnitude of the ellipsoidal error axes in the three directions was calculated to represent the overall positioning error. The ellipsoids for the PPP, PPP-DA, and PPP-GFS methods are shown in green, red, and blue, respectively, with their corresponding values displayed alongside each ellipsoid.

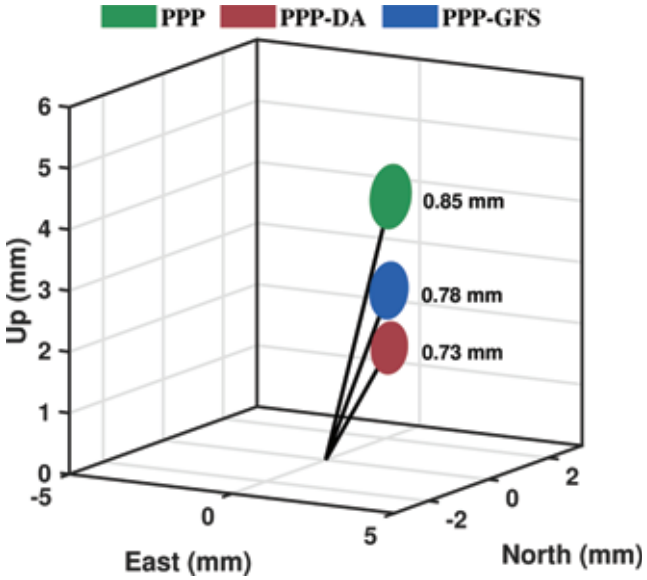

Figure 14. Illustration of the ellipsoidal errors for the HUEG station, derived from the three considered methods on January 1, 2021. The ellipsoids corresponding to the PPP, PPP-DA, and PPP-GFS methods are shown in green, red, and blue, respectively. Additionally, the black lines represent the error vectors for each method.

Referring to Figure 14, the ellipsoidal errors for the PPP and PPP-DA methods do not overlap and are clearly separated. For the HUEG station on January 1, 2021, the 3D positioning errors for the PPP, PPP-DA, and PPP-GFS methods are approximately 7.2, 5, and 5.8 millimeters, respectively. The PPP-DA method shows an improvement of about 2.2 millimeters compared to the PPP method. Given that the ellipsoidal errors for these two methods do not overlap, this 2.2-millimeter improvement can be considered statistically significant. Additionally, the lack of overlap between the ellipsoidal errors of the PPP-DA and PPP-GFS methods indicates that the 0.8-millimeter improvement is also statistically significant. Furthermore, Figure 14 highlights that the PPP-DA method has the smallest ellipsoid, reflecting the lower uncertainties achieved in all three directions compared to the other methods.

Similarly, we investigated the significance of the improvements of the PPP-DA and PPP-GFS methods compared to PPP, as well as PPP-DA compared to PPP-GFS for each station over the entire year 2021. The three evaluation cases are defined as follows:

- PPP/DA: The percentage of cases where the ellipsoidal errors from the PPP and PPP-DA methods did not overlap, and the 3D positioning error of PPP-DA is lower than that of PPP.
- PPP/GFS: The percentage of cases where the ellipsoidal errors from the PPP and PPP-GFS methods did not overlap, and the 3D positioning error of PPP-GFS is lower than that of PPP.
- GFS/DA: The percentage of cases where the ellipsoidal errors from the PPP-DA and PPP-GFS methods did not overlap, and the 3D positioning error of PPP-DA is lower than that of PPP-GFS.

The numerical results of this evaluation are shown in Figure 15, where the percentages of significance for the PPP/DA, PPP/GFS, and GFS/DA cases are represented by red, blue, and green bars, respectively.

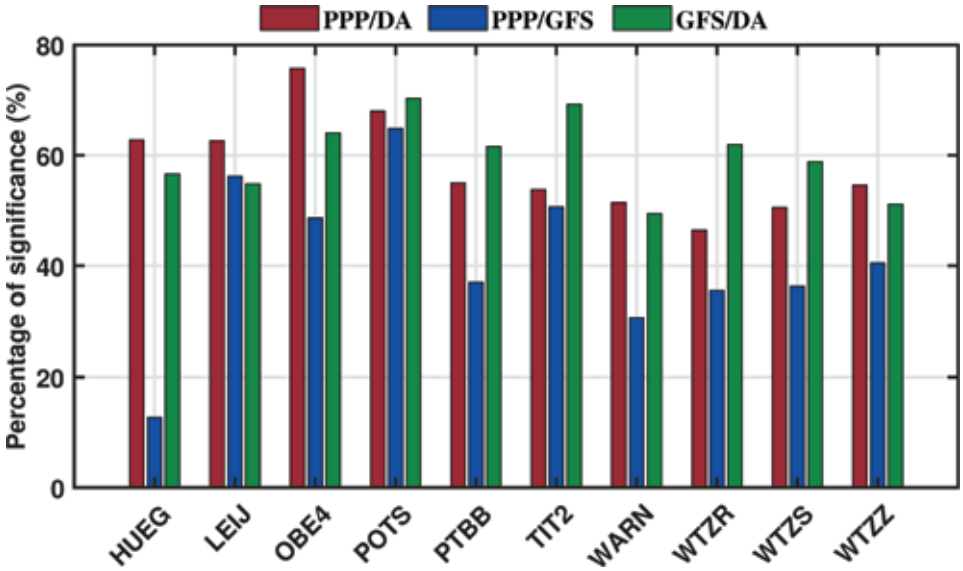

Figure 15. Percentage of significance for each station in 2021, comparing three cases: PPP/DA (red bars), PPP/GFS (blue bars), and GFS/DA (green bars). Significance is determined by non-overlapping ellipsoidal errors and lower 3D positioning errors.

Referring to Figure 15, the mean percentage of significance for the PPP/DA, PPP/GFS, and GFS/DA cases are approximately 58%, 41%, and 60%, respectively. Based on these values, in 58% of cases, the PPP-DA method not only outperformed the conventional PPP method, but this improvement is also statistically significant. Furthermore, according to the GFS/DA comparison, the PPP-DA method demonstrates both improvement and significance over the PPP-GFS method in 60% of cases.

To further substantiate the significance of the positional improvements offered by the PPP-DA method, a statistical analysis based on 95% confidence intervals of 3D positioning errors was conducted across ten GNSS stations. For each method (conventional PPP, PPP-DA, and PPP-GFS) the mean and confidence bounds of the 3D error were computed per station, allowing a clear comparison of accuracy levels. Paired t-tests (Moore et al., 2009) were then applied to the mean errors across stations to assess the significance of observed differences. The paired t-test was used to assess whether the difference in 3D positioning errors between the methods is statistically significant. The 95% confidence intervals represent the range within which the true mean error is expected to lie for each station (Moore et al., 2009). The 95% confidence interval ranges for the mean 3D positioning errors of each method are illustrated in Figure 16 , highlighting the variation in performance across all evaluated stations.

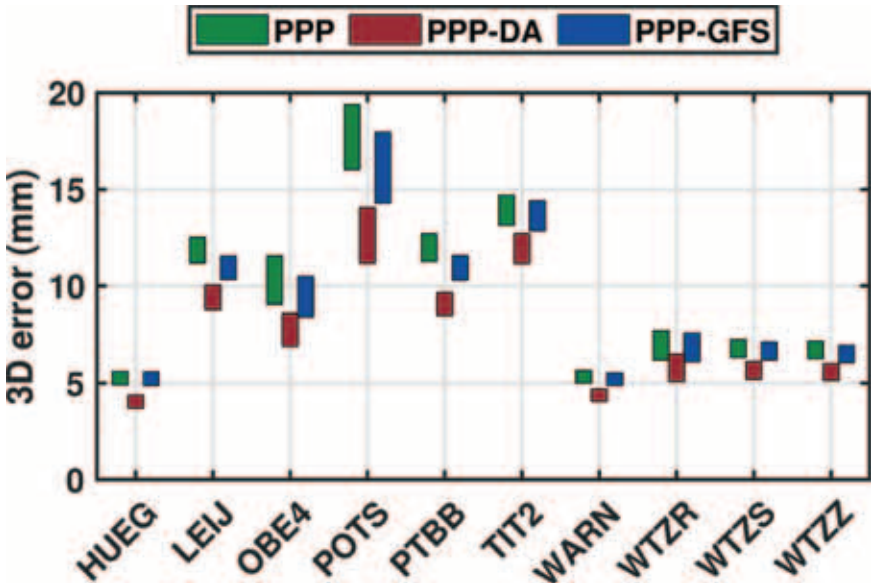

Figure 16. Comparison of 95% confidence intervals for mean 3D positioning errors across all evaluated stations using three methods: conventional PPP (green bars), PPP-DA (red bars), and PPP-GFS (blue bars).

Referring to Figure 16, it is evident that, for nearly all stations, the 95% confidence intervals of the PPP-DA method are not only narrower but also show minimal overlap with those of the conventional PPP and PPP-GFS methods. This consistent separation strongly suggests that the improvements in positioning accuracy achieved by PPP-DA are statistically significant. On average, across all stations, the 95% confidence intervals of the 3D positioning error for PPP-DA and PPP are [6.9, 8.8] mm and [8.9, 10.2] mm, respectively, further confirming the significant reduction in positioning error provided by the PPP-DA approach.

4.2.2. Convergence time comparison

To fully assess the performance of the PPP-DA and PPP-GFS methods, it is important to compare not only their positioning accuracy but also their convergence time. Convergence time is defined as the period required for the positioning solution to reach and consistently maintain a predefined level of accuracy. Specifically, it refers to the time taken for the positioning error in each direction to remain below a specified threshold (e.g., 10 millimeters) for a continuous period. For this evaluation, the convergence time required to achieve 10-millimeter accuracy was calculated for each station over the entire year 2021, across all days. Figure 17 presents the convergence time for the horizontal (a), vertical (b), and 3D positioning (c) errors at each station, with green, red, and blue bars representing results from the PPP, PPP-DA, and PPP-GFS methods, respectively.

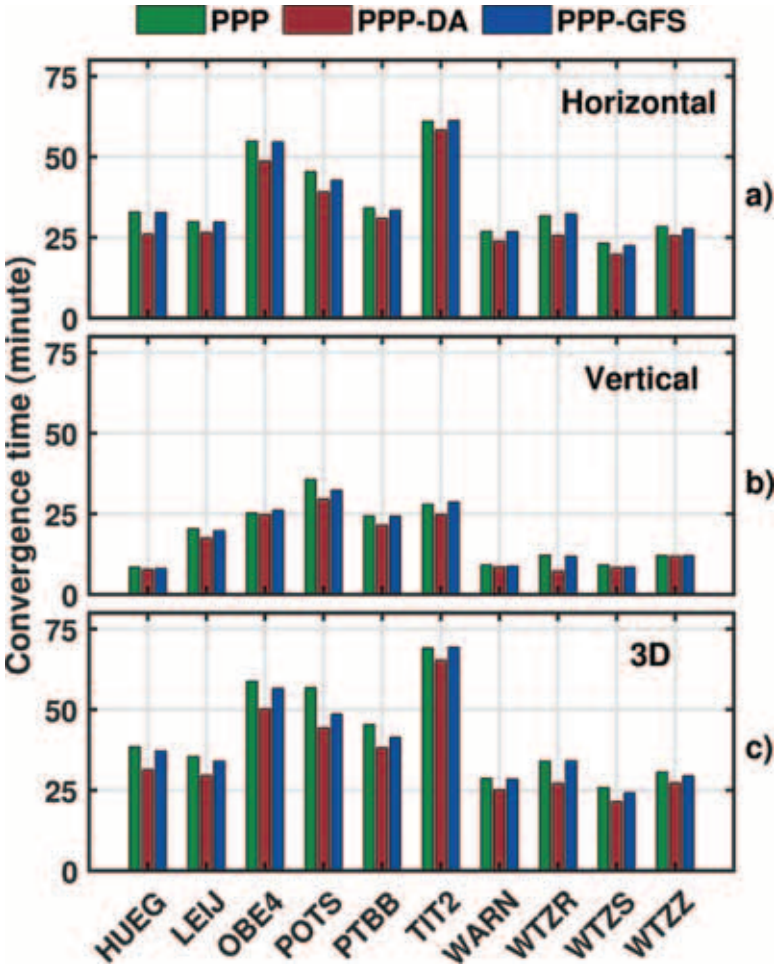

Figure 17. Convergence time comparison for horizontal (a), vertical (b), and 3D positioning (c) errors across all stations over the entire year 2021. The bars represent the time required for each method to achieve and maintain a positioning error below 10 millimeters. Results for the PPP, PPP-DA, and PPP-GFS methods are shown in green, red, and blue bars, respectively.

Referring Figure 17a, the mean convergence times for the horizontal positioning error using the PPP, PPP-DA, and PPP-GFS methods are approximately 37, 32, and 36 minutes, respectively. This indicates an improvement of 13% and 11% in the PPP-DA method over the conventional PPP and PPP-GFS methods, respectively. Moreover, the mean vertical convergence time (Figure 17b) for the PPP-DA method is approximately 16 minutes, representing an improvement of about 16% compared to the PPP method and 11% compared to the PPP-GFS method. Comparing the vertical positioning convergence time with the standard deviation of ZWD values in Figure 12, it is evident that the vertical Convergence time for each station shows a strong correlation with the corresponding ZWD variations at that station. This indicates that higher ZWD variability is associated with longer vertical convergence times. When comparing 3D positioning convergence times, the PPP-DA method demonstrates a convergence time of approximately 36 minutes. This is 16% faster than the PPP method, which has a convergence time of 43 minutes, and 12% faster than the PPP-GFS method, which converges in 41 minutes. Overall, it can be concluded that the PPP-DA method outperforms both the PPP and PPP-GFS methods in terms of both convergence time and positioning accuracy. Comparing the PPP and PPP-GFS methods, it

can be concluded that, similar to positioning performance, the PPP-GFS method demonstrates better performance
than the conventional PPP method.
When comparing these results with previous studies, Wilgan et al. (2017) reported convergence time reductions of approximately 13% for horizontal positioning and 20% for vertical positioning by integrating ZTD constraints from the WRF model into PPP. Similarly, Gong et al. (2024) observed reductions in convergence times of around 25% through WRF-based wet delay corrections. Yao et al. (2014) introduced a GNSS-based global Zenith Total Delay (ZTD) model as a pseudo-observation, achieving a 15% improvement in PPP convergence time. The convergence time reductions achieved in this study (approximately 16% for 3D positioning) are comparable, offering a lower computational cost alternative through the C/DA method. In the study by de Oliveira et al. (2017), it was reported that introducing an external atmospheric constraint led to improvements in convergence time of approximately 1%, 20%, and 5% in the east, north, and up components, respectively, when using only GPS observations. Moreover, the PPP-RTK experiment conducted by Song et al. (2022) demonstrated that incorporating ZWD constraints reduced the convergence time by approximately 5 minutes.
For further evaluation, we analyzed the convergence times required by the three implemented PPP methods to achieve different levels of accuracy. Figure 18 illustrates the average convergence times for each method in the horizontal (a), vertical (b), and 3D directions (3) across all stations during the evaluation period. In this figure, the convergence times for the PPP, PPP-DA, and PPP-GFS methods are represented by green, red, and blue bars, respectively.

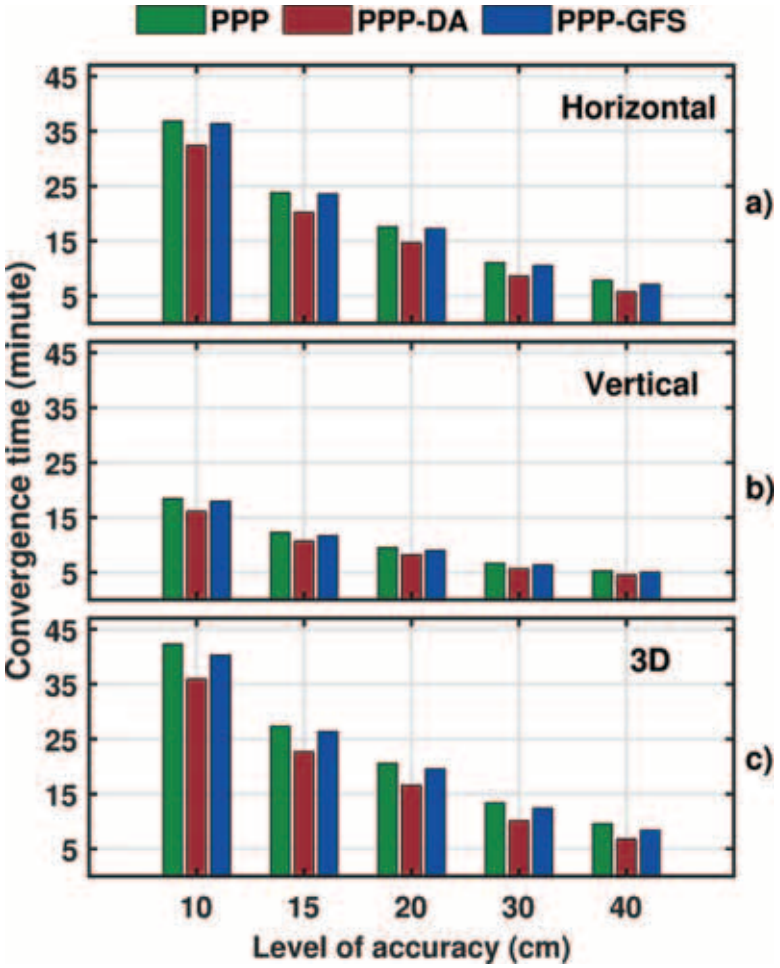

Figure 18. Mean convergence times for the PPP, PPP-DA, and PPP-GFS methods in the horizontal (a), vertical (b), and 3D directions (c), averaged over all stations during the evaluation period. Green, red, and blue bars represent the PPP, PPP-DA, and PPP-GFS methods, respectively.

According to Figure 18, the PPP-DA method consistently demonstrates a shorter convergence time compared to both PPP and PPP-GFS methods across all accuracy levels. Specifically, the PPP-DA method requires approximately 36 minutes to achieve a 10 cm accuracy in the 3D direction (Figure 18c), which decreases to about 7 minutes for a 40 cm accuracy level. Compared to the conventional PPP method, the PPP-DA method reduces the convergence time by approximately 6 minutes at the 10 cm accuracy level. However, this difference diminishes at higher accuracy thresholds, with the PPP-DA method requiring about 2.5 minutes less than the PPP method at the 40 cm accuracy level. These results highlight that integrating high-precision ZWD constraints is particularly effective for reducing convergence time in high-precision positioning applications. Furthermore, the convergence time reduction remains significant even at lower accuracy thresholds, underscoring the broader utility of the PPP-DA method.

A statistical analysis was conducted to evaluate the convergence time required to achieve 10 cm 3D positioning accuracy across 10 GNSS test stations. To assess the significance of performance differences among the evaluated methods—conventional PPP, PPP-DA, and PPP-GFS—paired t-tests were applied to the convergence time results across all stations. For each method, the mean convergence time and corresponding 95% confidence intervals were computed per station,

enabling a clear comparison of their convergence behaviors. The confidence intervals represent the expected range in which the true mean convergence time lies. The results of this analysis are illustrated in Figure 19, showing the variation in convergence performance across the evaluated stations and methods.

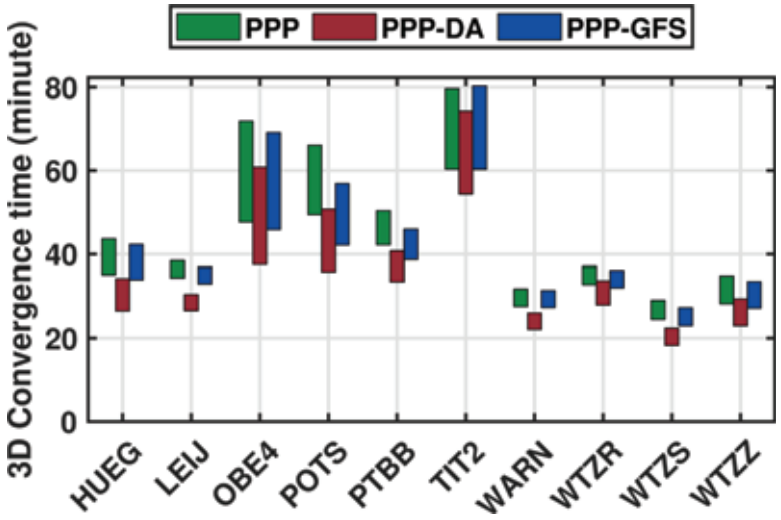

Figure 19. Comparison of 95% confidence intervals for mean 3D convergence time across all evaluated stations. The corresponding values for PPP, PPP-DA, and PPP-GFS are illustrated with green, red, and blue bars, respectively.

Referring to Figure 19, the analysis of 95% confidence intervals for mean 3D convergence times shows that both the PPP-DA and PPP-GFS methods consistently outperform the conventional PPP approach across all evaluated stations. Among these, the PPP-DA method achieves the shortest convergence times at most stations, underscoring the advantage of assimilating accurate ZWD constraints into the positioning process. Furthermore, for the majority of stations, the confidence intervals of convergence time for the PPP-DA method do not overlap with those of the PPP method, highlighting the statistical significance of the observed improvements. On average across all stations, the 95% confidence interval for convergence time is [30, 40] minutes for PPP-DA, compared to [38, 48] minutes for PPP, reflecting an average improvement of approximately 8 minutes.

5. Conclusions

A key challenge in enhancing the accuracy of Precise Point Positioning (PPP) lies in addressing the atmospheric wet delay caused by water vapor in the lower layers of the atmosphere. This delay significantly impacts the initialization and precision of satellite-based positioning systems. Despite their utility, existing empirical models often fail to capture the complex spatial and temporal variability of wet delays, making them less effective in applications requiring high precision. To overcome these limitations, this study proposes a novel Calibration and Data Assimilation (C/DA) framework aimed at improving ZWD estimation and prediction. The approach includes developing a regional atmospheric wet delay model based on Principal Component Analysis (PCA-ZWD), which serves as the foundational background model. Using EnKF, the model is further refined by incorporating GNSS-derived ZWD values, providing a

robust method for enhancing the representation of atmospheric wet delays in positioning applications. In comparison with the considered test stations, the estimated ZWD values using the C/DA method indicated an RMSE of approximately 0.83 centimeters which was 48%, 73%, and 72% lower compared to the GFS, GTrop, and PCA-ZWD models. Subsequently, the ZWD values estimated through the C/DA method were incorporated as constraints into the PPP method. The proposed framework was rigorously evaluated using GNSS observations from 10 IGS stations and over a one-year period. The results demonstrated that integrating ZWD corrections into the PPP method reduced the 3D positioning error by approximately 21% compared to the conventional PPP and 16% compared to the GFS-PPP method, with the majority of these improvements attributed to enhancements in the vertical direction. The convergence time required to achieve a 10-centimeter level of accuracy for the PPP-DA method was approximately 36 minutes, reflecting a reduction of 16% compared to the PPP method and 12% compared to the PPP-GFS method. Additionally, when comparing convergence times across various accuracy thresholds, the PPP-DA method consistently exhibited shorter convergence times than the PPP method, even at a 40-centimeter accuracy level. These results underscore the significant potential of the C/DA framework in enhancing PPP performance for high-precision geodetic applications.

Future studies could apply the proposed C/DA and PPP-DA methods in other geographic regions with diverse topographic and atmospheric conditions to evaluate their robustness and generalizability. Furthermore, future work may explore the assimilation of additional observational sources, such as remote sensing satellite data, alongside GNSS observations to assess the advantages of multi-source data fusion in enhancing ZWD estimation. Lastly, investigating the potential for real-time implementation of the C/DA method, particularly for real-time PPP applications, presents a valuable direction. Since real-time PPP depends on accurate and low-latency tropospheric delay estimates, assessing the performance of the proposed method under real-time constraints would offer important insights into its operational applicability.

Acknowledgments

The authors express their sincere gratitude to the National Center for Atmospheric Research (NCAR) and the Copernicus Climate Change Service for providing the GFS and ERA5 atmospheric data, respectively. They also extend their heartfelt thanks to the Nevada Geodetic Laboratory (NGL) for supplying the GNSS-derived Zenith Wet Delay (ZWD) values. Appreciation is further extended to the NASA CDDIS archive for providing raw GNSS observations and related products used for PPP processing, and to the University of Wyoming for offering access to upper-air radiosonde observations. The authors also acknowledge the developers of the GTrop model for making its source code publicly available for research and comparison.

Open Research

Data Availability Statement

Atmospheric parameters from the GFS model were retrieved from the NCAR Research Data Archive (https://rda.ucar.edu/datasets/d084001/). Zenith Wet Delay (ZWD) values were obtained

from the Nevada Geodetic Laboratory (http://geodesy.unr.edu/gps_timeseries/trop/). ERA5 datasets were sourced from the Copernicus Climate Data Store (https://cds.climate.copernicus.eu/datasets/reanalysis-era5-pressure-levels?tab=download) (Hersbach et al., 2020). Raw GNSS observations and related products used for PPP processing were acquired from the CDDIS archive (https://cddis.nasa.gov/archive/gnss/) (Noll, 2010). Radiosonde observations were retrieved from the University of Wyoming's upper-air data archive (http://weather.uwyo.edu/upperair/sounding.shtml/). The GTrop model (Sun et al., 2019) was also used for comparison, with its source code accessed via https://github.com/sun1753814280/GTrop/.

References

Al-Fanek, O. J. S. (2013). *Ionospheric imaging for Canadian polar regions*. In. Retrieved from https://prism.ucalgary.ca doi:10.11575/PRISM/26672.

Bertino, L., Evensen, G., & Wackernagel, H. (2003). Sequential data assimilation techniques in oceanography. *International Statistical Review, 71*(2), 223-241. https://doi.org/10.1111/j.1751-5823.2003.tb00194.x.

Blewitt, G., Hammond, W., & Kreemer, C. (2018). Harnessing the GPS data explosion for interdisciplinary science [Dataset]. *Eos, 99*(2), e2020943118. https://doi.org/10.1029/2018EO104623.

Boehm, J., Werl, B., & Schuh, H. (2006). Troposphere mapping functions for GPS and very long baseline interferometry from European Centre for Medium-Range Weather Forecasts operational analysis data. *Journal of Geophysical Research: Solid Earth, 111*(B2). https://doi.org/10.1029/2005JB003629.

Collins, J. P., & Langley, R. B. (1997). *A tropospheric delay model for the user of the wide area augmentation system*. In Vol. 20. Retrieved from http://131.202.94.44/papers.pdf/waas.tropo.oct96.pdf

de Oliveira Jr, P., Morel, L., Fund, F., Legros, R., Monico, J., Durand, S., & Durand, F. (2017). Modeling tropospheric wet delays with dense and sparse network configurations for PPP-RTK. *GPS solutions, 21*(1), 237-250. https://doi.org/10.1007/s10291-016-0518-0.

Dee, D. P., Uppala, S. M., Simmons, A. J., Berrisford, P., Poli, P., Kobayashi, S., et al. (2011). The ERA-Interim reanalysis: Configuration and performance of the data assimilation system. *Quarterly Journal of the Royal Meteorological Society, 137*(656), 553-597. https://doi.org/10.1002/qj.828.

Dehvari, M., Farzaneh, S., & Forootan, E. (2023). Developing Iran's empirical zenith wet delay model (IR-ZWD). *Journal of Atmospheric and Solar-Terrestrial Physics*, 106163. https://doi.org/10.1016/j.jastp.2023.106163.

Dehvari, M., Farzaneh, S., & Forootan, E. (2024a). Assessment of ZWD field predictions using the dynamic mode decomposition method. *GPS solutions, 28*(3), 145. https://doi.org/10.1007/s10291-024-01692-w.

Dehvari, M., Farzaneh, S., & Forootan, E. (2024b). Ensemble based estimation of wet refractivity indices using a functional model approach. *Earth and Space Science, 11*(10), e2023EA003453. https://doi.org/10.1029/2023EA003453.

Evensen, G. (2003). The ensemble Kalman filter: Theoretical formulation and practical implementation. *Ocean dynamics, 53*, 343-367. https://doi.org/10.1007/s10236-003-0036-9.

Forootan, E., Dehvari, M., Farzaneh, S., & Karimi, S. (2023). Improving the Wet Refractivity Estimation Using the Extremely Learning Machine (ELM) Technique. *Atmosphere, 14*(1), 112. https://doi.org/10.3390/atmos14010112.

Forootan, E., Dehvari, M., Farzaneh, S., & Khaniani, A. S. (2021). A functional modelling approach for reconstructing 3 and 4 dimensional wet refractivity fields in the lower atmosphere using GNSS measurements. *Advances in Space Research, 68*(10), 4024-4038. https://doi.org/10.1016/j.asr.2021.08.012.

Forootan, E., Farzaneh, S., Dehvari, M., Retegui-Schiettekatte, L., & Schumacher, M. (2024). *Sequential calibration and data assimilation for predicting atmospheric variability*. Retrieved from https://doi.org/10.5194/egusphere-egu24-5567

Forootan, E., Farzaneh, S., Kosary, M., Schmidt, M., & Schumacher, M. (2021). A simultaneous calibration and data assimilation (C/DA) to improve NRLMSISE00 using thermospheric neutral density (TND) from space-borne accelerometer measurements. *Geophysical Journal International, 224*(2), 1096-1115. https://doi.org/10.1093/gji/ggaa507.

Glaner, M. F., & Weber, R. (2023). An open-source software package for Precise Point Positioning: raPPPid [Software]. *GPS solutions, 27*(4), 174. https://doi.org/10.1007/s10291-023-01488-4.

Gong, Y., Liu, Z., Yu, S., Chan, P. W., & Hon, K. K. (2024). Improving GNSS PPP performance in the South China under different weather conditions by using the Weather Research and Forecasting (WRF) model-derived wet delay corrections. *Earth and Space Science, 11*(3), e2023EA003136. https://doi.org/10.1029/2023EA003136.

Haji-Aghajany, S., Amerian, Y., & Verhagen, S. (2020). B-spline function-based approach for GPS tropospheric tomography. *GPS solutions, 24*(3), 1-12. https://doi.org/10.1007/s10291-020-01005-x.

Herring, T., King, R., & McClusky, S. (2010). Introduction to gamit/globk [Software]. *Massachusetts Institute of Technology, Cambridge, Massachusetts, 400*, 401.

Hersbach, H., Bell, B., Berrisford, P., Hirahara, S., Horányi, A., Muñoz-Sabater, J., et al. (2020). The ERA5 global reanalysis [Dataset]. *Quarterly Journal of the Royal Meteorological Society, 146*(730), 1999-2049. https://doi.org/10.1002/qj.3803.

Hofmann-Wellenhof, B., Lichtenegger, H., & Wasle, E. (2007). *GNSS–global navigation satellite systems: GPS, GLONASS, Galileo, and more*. In. doi:https://doi.org/10.1007/978-3-211-73017-1.

Houtekamer, P. L., & Zhang, F. (2016). Review of the ensemble Kalman filter for atmospheric data assimilation. *Monthly Weather Review, 144*(12), 4489-4532. https://doi.org/10.1175/MWR-D-15-0440.1.

Jolliffe, I. (2005). Principal component analysis. *Encyclopedia of statistics in behavioral science*.

Jolliffe, I. T., & Cadima, J. (2016). Principal component analysis: a review and recent developments. *Philosophical transactions of the royal society A: Mathematical, Physical and Engineering Sciences, 374*(2065), 20150202. https://doi.org/10.1098/rsta.2015.0202.

Kosary, M., Forootan, E., Farzaneh, S., & Schumacher, M. (2022). A sequential calibration approach based on the ensemble Kalman filter (C-EnKF) for forecasting total electron content (TEC). *Journal of Geodesy, 96*(4), 29. https://doi.org/10.1007/s00190-022-01623-y.

Kouba, J., & Héroux, P. (2001). Precise point positioning using IGS orbit and clock products. *GPS solutions, 5*, 12-28. https://doi.org/10.1007/PL00012883.

Landskron, D., & Böhm, J. (2018). VMF3/GPT3: refined discrete and empirical troposphere mapping functions [Software]. *Journal of Geodesy, 92*(4), 349-360. https://doi.org/10.1007/s00190-017-1066-2.

Leick, A. (2015). *GPS satellite surveying*: Wiley.

Li, J., Li, F., Liu, L., Huang, L., Zhou, L., & He, H. (2022). A calibrated GPT3 (CGPT3) model for the site-specific zenith hydrostatic delay estimation in the Chinese Mainland and its surrounding areas. *Remote Sensing, 14*(24), 6357. https://doi.org/10.3390/rs14246357.

Li, X., Zhang, X., & Ge, M. (2011). Regional reference network augmented precise point positioning for instantaneous ambiguity resolution. *Journal of Geodesy, 85*, 151-158. https://doi.org/10.1007/s00190-010-0424-0.

Limberger, M. (2015). *Ionosphere modeling from GPS radio occultations and complementary data based on B-splines*. In. Retrieved from https://nbn-resolving.de/urn/resolver.pl?urn:nbn:de:bvb:91-diss-20151006-1254715-1-1

Lu, C., Li, X., Zus, F., Heinkelmann, R., Dick, G., Ge, M., et al. (2017). Improving BeiDou real-time precise point positioning with numerical weather models. *Journal of Geodesy, 91*, 1019-1029. https://doi.org/10.1007/s00190-017-1005-2.

Ma, Y., Liu, H., Xu, G., & Lu, Z. (2021). Empirical orthogonal function analysis and modeling of global tropospheric delay spherical harmonic coefficients. *Remote Sensing, 13*(21), 4385. https://doi.org/10.3390/rs13214385.

Mirmohammadian, F., Asgari, J., Verhagen, S., & Amiri-Simkooei, A. (2022). Multi-GNSS-weighted interpolated tropospheric delay to improve long-baseline RTK positioning. *Sensors, 22*(15), 5570. https://doi.org/10.3390/s22155570.

Moore, D. S., McCabe, G. P., & Craig, B. A. (2009). *Introduction to the Practice of Statistics* (Vol. 4): WH Freeman New York.

National Centers for Environmental Prediction/National Weather Service/NOAA/U.S. Department of Commerce. (2015). NCEP GFS 0.25 Degree Global Forecast Grids Historical Archive (Updated daily) [Dataset]. Research Data Archive at the National Center for Atmospheric Research, Computational and Information Systems Laboratory. https://doi.org/10.5065/D65D8PWK.

Noll, C. E. (2010). The crustal dynamics data information system: A resource to support scientific analysis using space geodesy [Dataset]. *Advances in Space Research, 45*(12), 1421-1440. https://doi.org/10.1016/j.asr.2010.01.018.

1006 Schmidt, M., Dettmering, D., Mößmer, M., Wang, Y., & Zhang, J. (2011). Comparison of spherical harmonic and B
1007 spline models for the vertical total electron content. *Radio Science, 46*(6).
1008 https://doi.org/10.1029/2010RS004609.
1009 Skamarock, W. C., Klemp, J. B., Dudhia, J., Gill, D. O., Barker, D. M., Duda, M. G., et al. (2008). A description of
1010 the advanced research WRF version 3. *NCAR technical note, 475*, 113.
1011 http://dx.doi.org/10.5065/D68S4MVH.
1012 Smith, P., Thornhill, G., Dance, S., Lawless, A., Mason, D., & Nichols, N. (2013). Data assimilation for state and
1013 parameter estimation: application to morphodynamic modelling. *Quarterly Journal of the Royal*
1014 *Meteorological Society, 139*(671), 314-327. https://doi.org/10.1002/qj.1944.
1015 Song, C., Ma, H., Zhu, H., Wu, B., & Shen, N. (2022). External tropospheric corrections by using kriging
1016 interpolation for improving PPP-RTK positioning solutions. *Remote Sensing, 14*(15), 3747.
1017 https://doi.org/10.3390/rs14153747.
1018 Subirana, J. S., Hernandez-Pajares, M., & Zornoza, J. e. M. J. (2013). *GNSS Data Processing: Fundamentals and*
1019 *Algorithms*: European Space Agency.
1020 Sun, Z., Zhang, B., & Yao, Y. (2019). A global model for estimating tropospheric delay and weighted mean
1021 temperature developed with atmospheric reanalysis data from 1979 to 2017 [Software]. *Remote Sensing,*
1022 *11*(16), 1893. https://doi.org/10.3390/rs11161893.
1023 Tang, J., Zhang, S., Huo, X., & Wu, X. (2022). Ionospheric Assimilation of GNSS TEC into IRI Model Using a
1024 Local Ensemble Kalman Filter. *Remote Sensing, 14*(14), 3267. https://doi.org/10.3390/rs14143267.
1025 Wilgan, K., Hadas, T., Hordyniec, P., & Bosy, J. (2017). Real-time precise point positioning augmented with high-
1026 resolution numerical weather prediction model. *GPS solutions, 21*, 1341-1353.
1027 https://doi.org/10.1007/s10291-017-0617-6.
1028 Yao, Y., Hu, Y., Yu, C., Zhang, B., & Guo, J. (2016). An improved global zenith tropospheric delay model GZTD2
1029 considering diurnal variations. *Nonlinear processes in geophysics, 23*(3), 127-136.
1030 https://doi.org/10.5194/npg-23-127-2016.
1031 Yao, Y., Yu, C., & Hu, Y. (2014). A new method to accelerate PPP convergence time by using a global zenith
1032 troposphere delay estimate model. *The Journal of Navigation, 67*(5), 899-910.
1033 https://doi.org/10.1017/S0373463314000265.
1034

Figure 1.

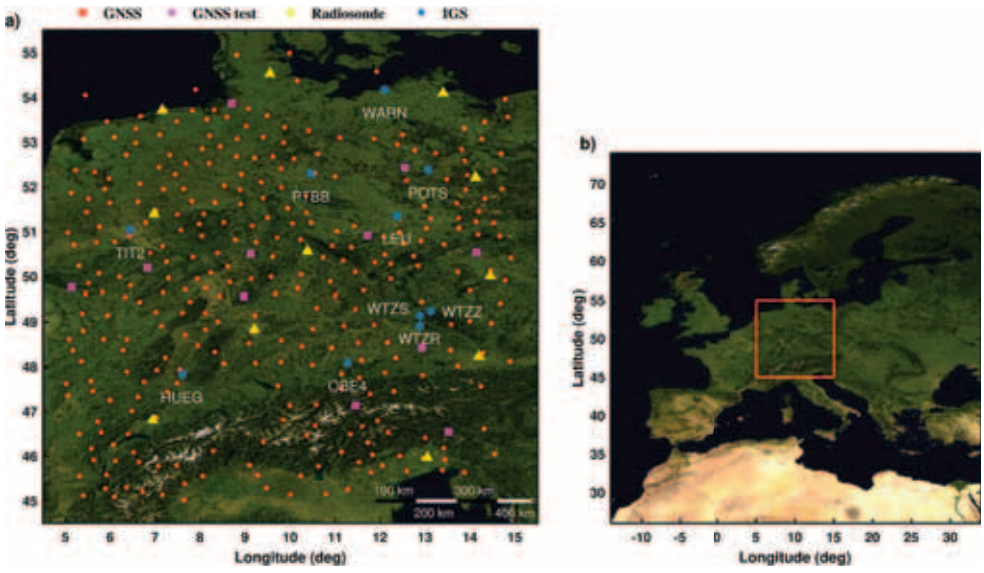
a)
GNSS
GNSS test
Radiosonde
IGS
WARN
PTB8
POTS
LEIJ
TITZ
WTZS
WTZZ
WTZR
RUEG
OBE4
100 km
200 km
400 km
Latitude (deg)
Longitude (deg)
b)
Latitude (deg)
Longitude (deg)

Figure 2.

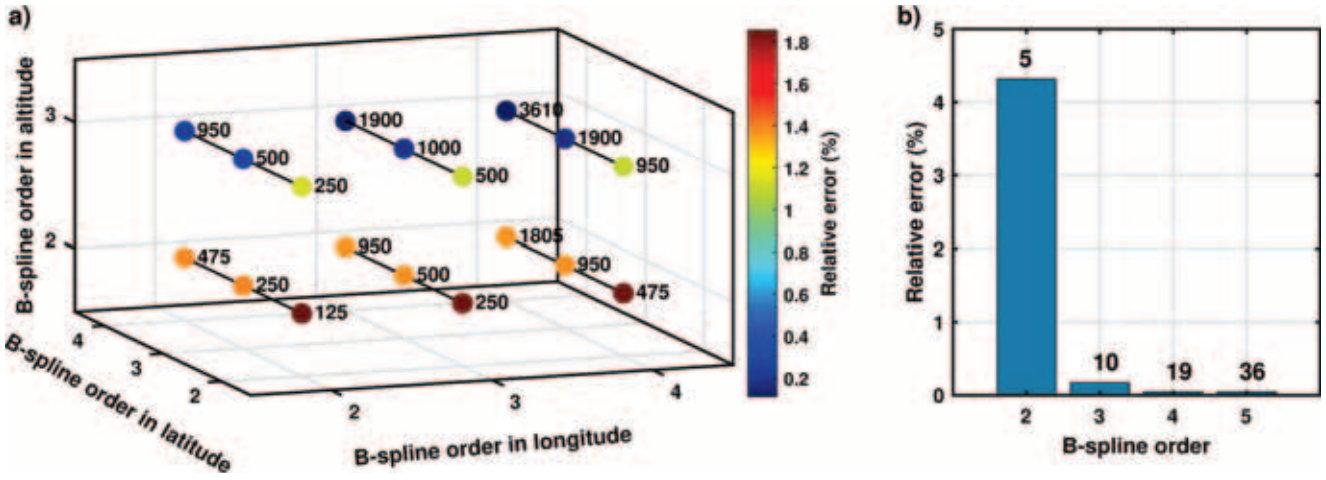
a)
B-spline order in altitude
B-spline order in latitude
B-spline order in longitude
Relative error (%)
950
500
250
1900
1000
500
3610
1900
950
475
250
125
950
500
250
1805
950
475
b)
Relative error (%)
B-spline order
5
10
19
36

Figure 3.

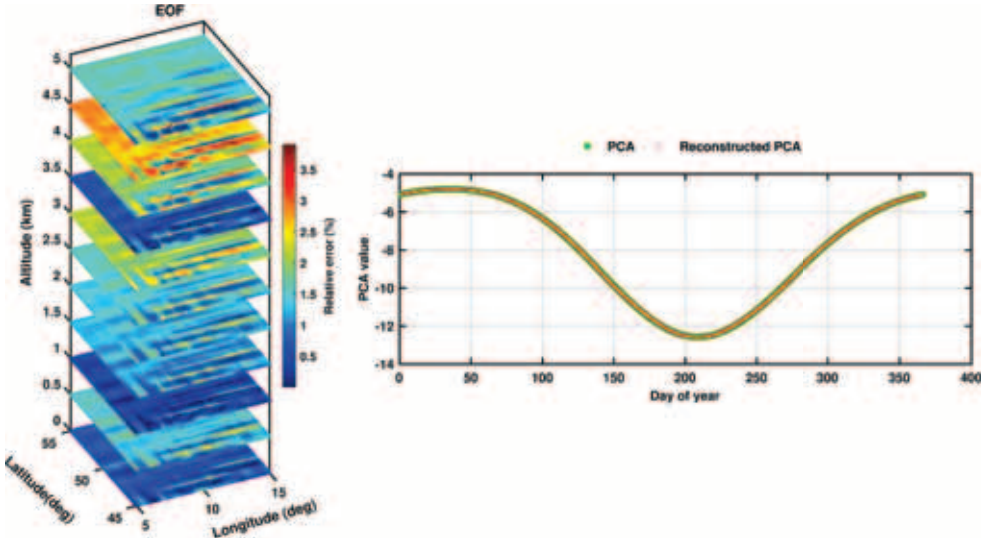
EOF
Altitude (km)
Latitude(deg)
Longitude (deg)
Relative error (%)
PCA
Reconstructed PCA
PCA value
Day of year

Figure 4.

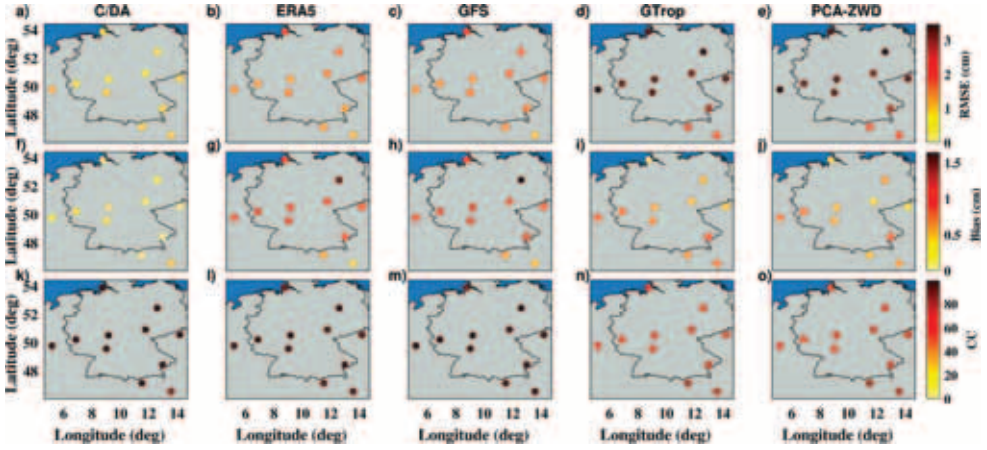
a)
C/DA
b)
ERA5
c)
GFS
d)
GTrop
e)
PCA-ZWD
f)
g)
h)
i)
j)
k)
l)
m)
n)
o)
Latitude (deg)
54
52
50
48
6 8 10 12 14
Longitude (deg)
RMSE (cm)
3
2
1
0
Bias (cm)
1.5
1
0.5
0
CC
80
60
40
20
0

Figure 5.

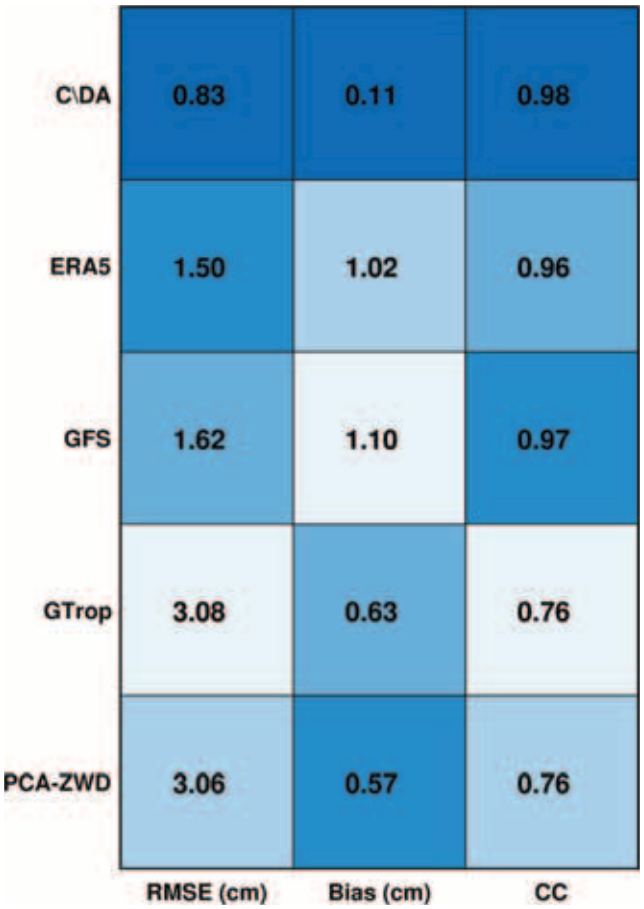
C\DA
0.83
0.11
0.98
ERA5
1.50
1.02
0.96
GFS
1.62
1.10
0.97
GTrop
3.08
0.63
0.76
PCA-ZWD
3.06
0.57
0.76
RMSE (cm)
Bias (cm)
CC

Figure 6.

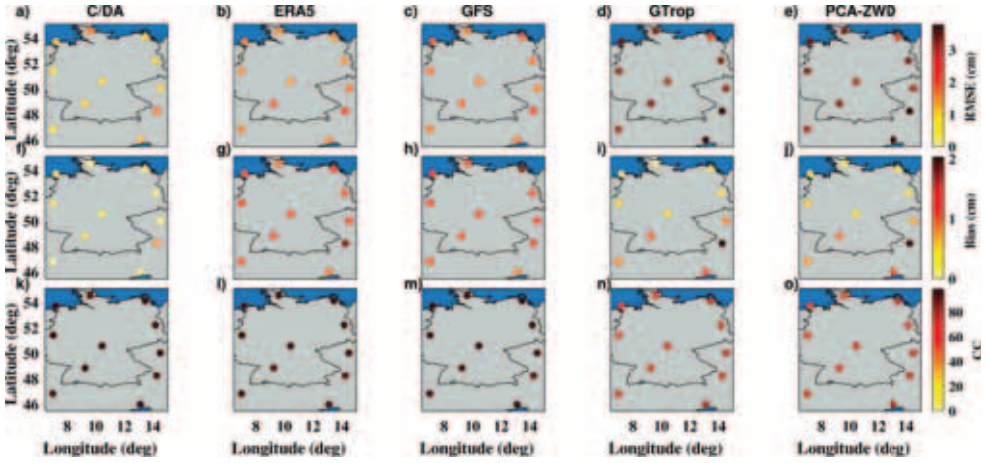
a) C/DA
b) ERA5
c) GFS
d) GTrop
e) PCA-ZWD
f)
g)
h)
i)
j)
k)
l)
m)
n)
o)
Latitude (deg)
54
52
50
48
46
8 10 12 14
Longitude (deg)
RMSE (cm)
Bias (cm)
CC

Figure 7.

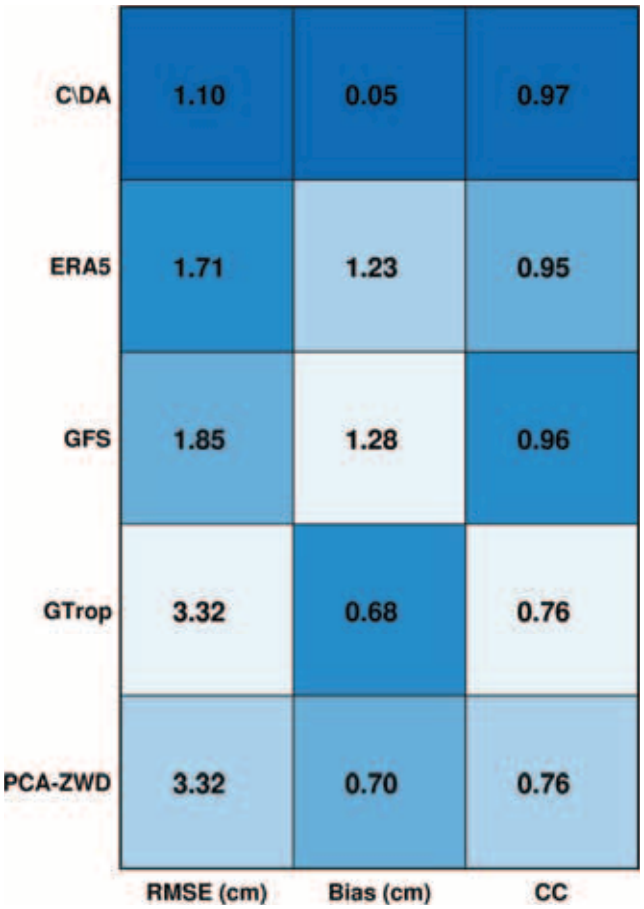
C\DA
1.10
0.05
0.97
ERA5
1.71
1.23
0.95
GFS
1.85
1.28
0.96
GTrop
3.32
0.68
0.76
PCA-ZWD
3.32
0.70
0.76
RMSE (cm)
Bias (cm)
CC

Figure 8.

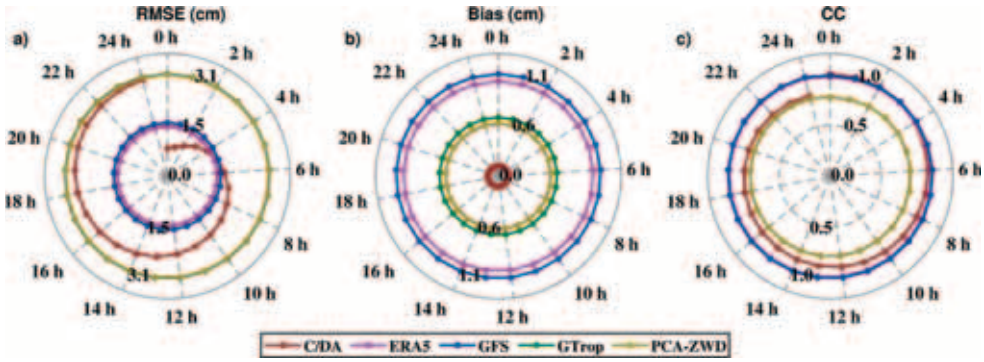
a)
RMSE (cm)
0 h
2 h
4 h
6 h
8 h
10 h
12 h
14 h
16 h
18 h
20 h
22 h
24 h
3.1
1.5
0.0
1.5
3.1
b)
Bias (cm)
1.1
0.6
0.0
0.6
1.1
c)
CC
1.0
0.5
0.0
0.5
1.0
C/DA
ERA5
GFS
GTrop
PCA-ZWD

Figure 9.

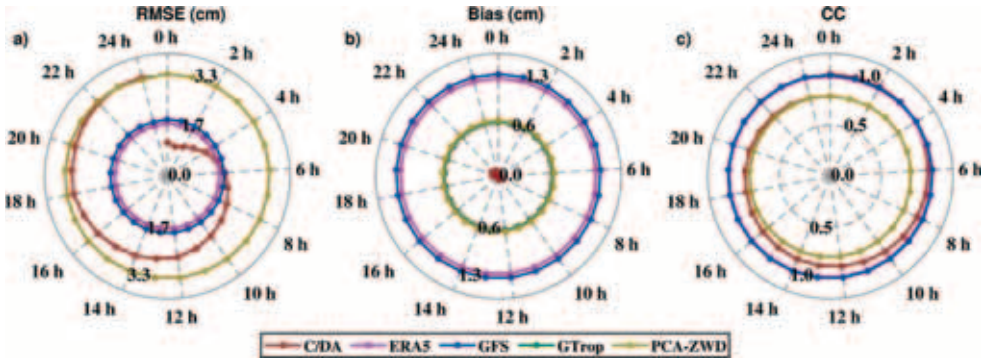
a)
RMSE (cm)
0 h
2 h
4 h
6 h
8 h
10 h
12 h
14 h
16 h
18 h
20 h
22 h
24 h
3.3
1.7
0.0
1.7
3.3
b)
Bias (cm)
1.3
0.6
0.0
0.6
1.3
c)
CC
1.0
0.5
0.0
0.5
1.0
C/DA
ERA5
GFS
GTrop
PCA-ZWD

Figure 10.

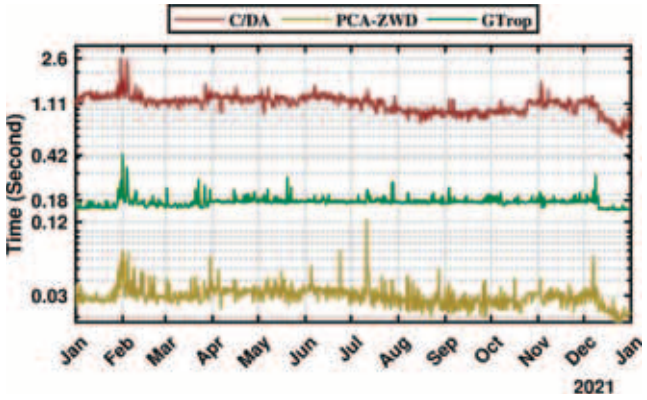
C/DA
PCA-ZWD
GTrop
Time (Second)
2.6
1.11
0.42
0.18
0.12
0.03
Jan
Feb
Mar
Apr
May
Jun
Jul
Aug
Sep
Oct
Nov
Dec
Jan
2021

Figure 11.

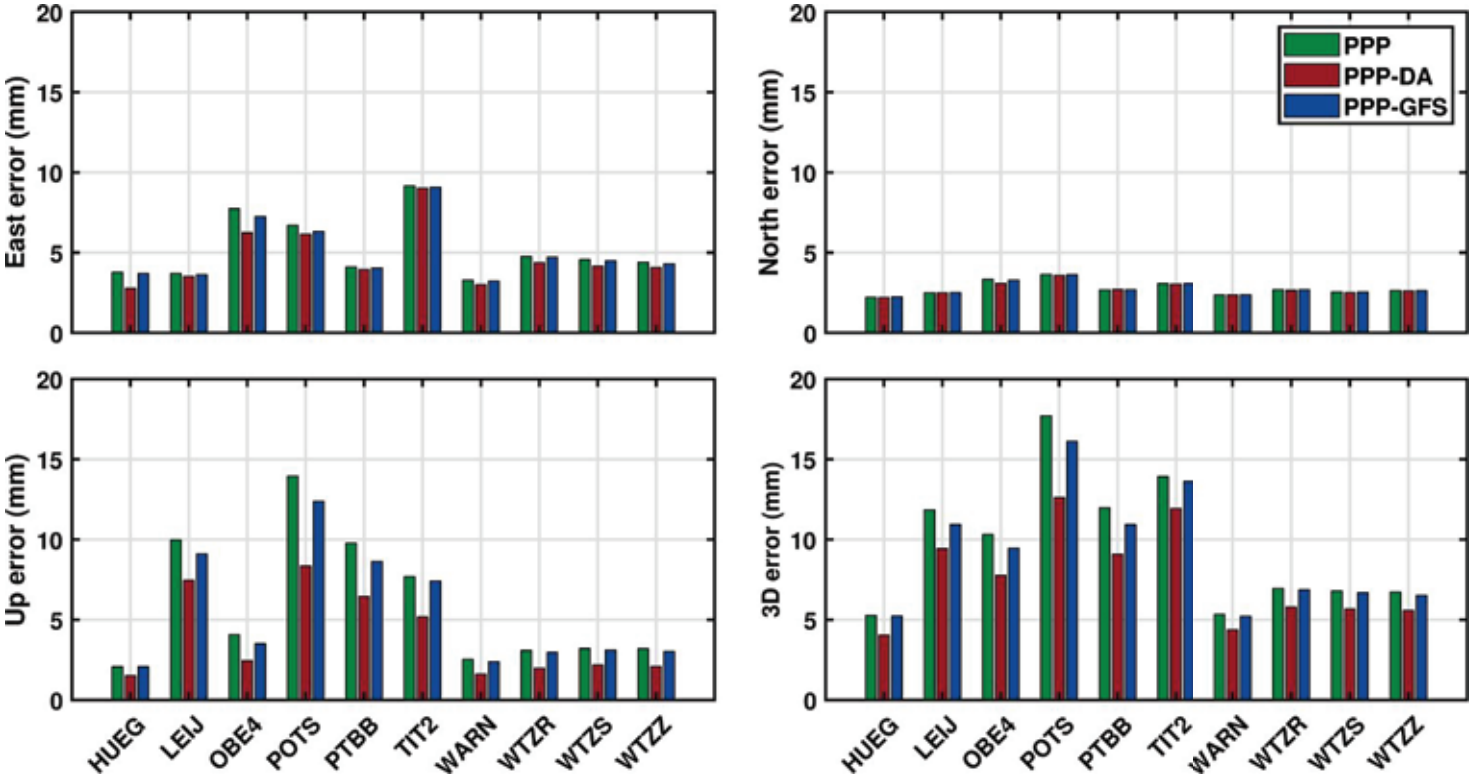
East error (mm)
North error (mm)
Up error (mm)
3D error (mm)
PPP
PPP-DA
PPP-GFS
0
5
10
15
20
HUEG
LEIJ
OBE4
POTS
PTBB
TIT2
WARN
WTZR
WTZS
WTZZ

Figure 12.

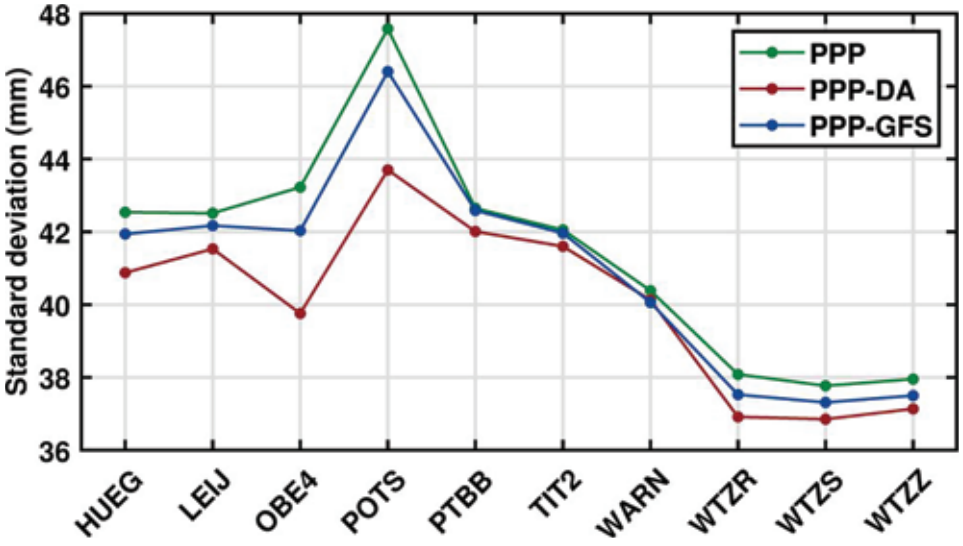
Standard deviation (mm)
48
46
44
42
40
38
36
PPP
PPP-DA
PPP-GFS
HUEG
LEIJ
OBE4
POTS
PTBB
TIT2
WARN
WTZR
WTZS
WTZZ

Figure 13.

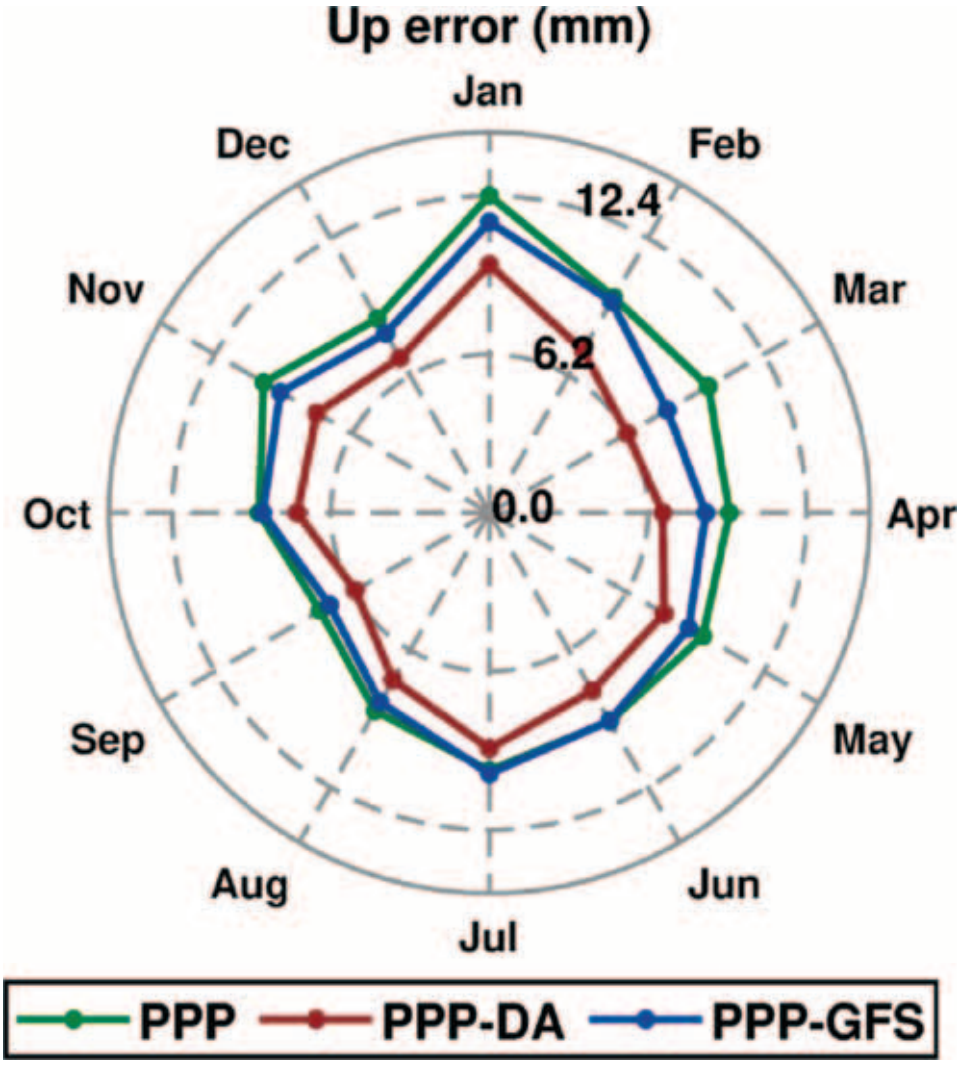
Up error (mm)
Jan
Feb
Mar
Apr
May
Jun
Jul
Aug
Sep
Oct
Nov
Dec
12.4
6.2
0.0
PPP
PPP-DA
PPP-GFS

Figure 14.

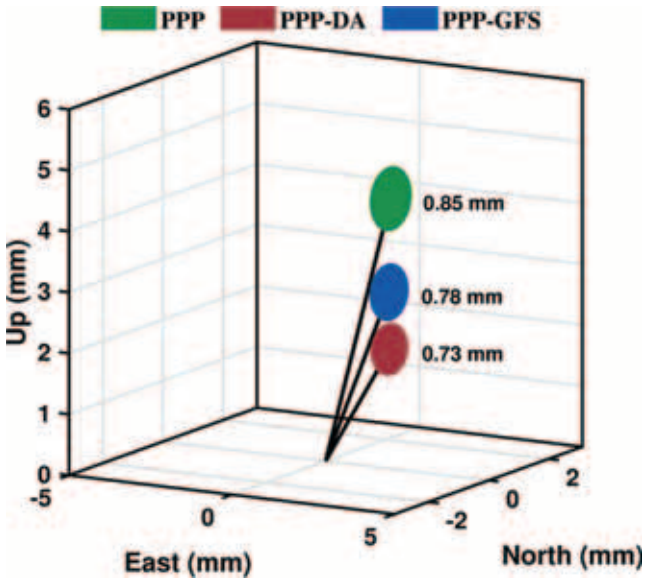
PPP
PPP-DA
PPP-GFS
0.85 mm
0.78 mm
0.73 mm
Up (mm)
6
5
4
3
2
1
0
-5
0
5
East (mm)
-2
0
2
North (mm)

Figure 15.

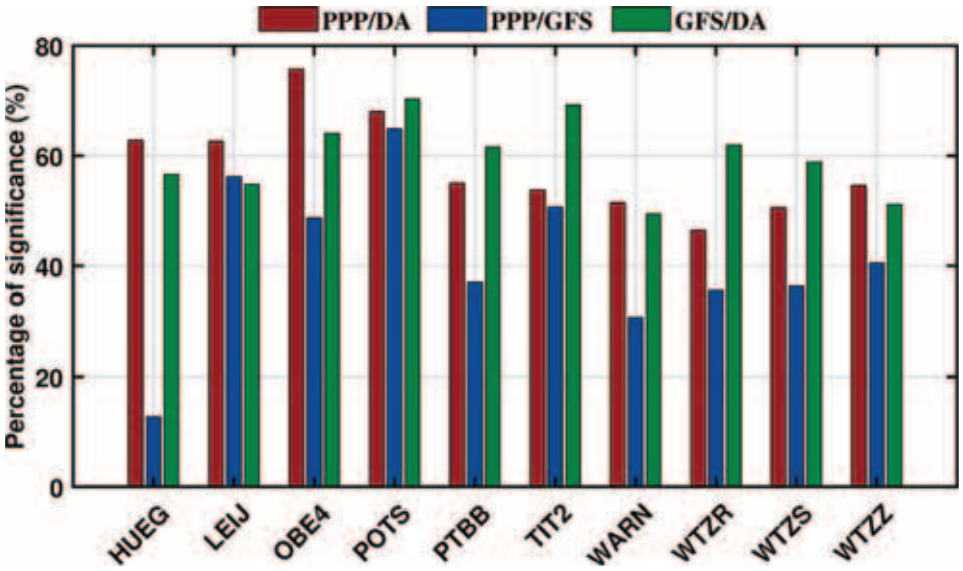
PPP/DA
PPP/GFS
GFS/DA
Percentage of significance (%)
0
20
40
60
80
HUEG
LEIJ
OBE4
POTS
PTBB
TIT2
WARN
WTZR
WTZS
WTZZ

Figure 16.

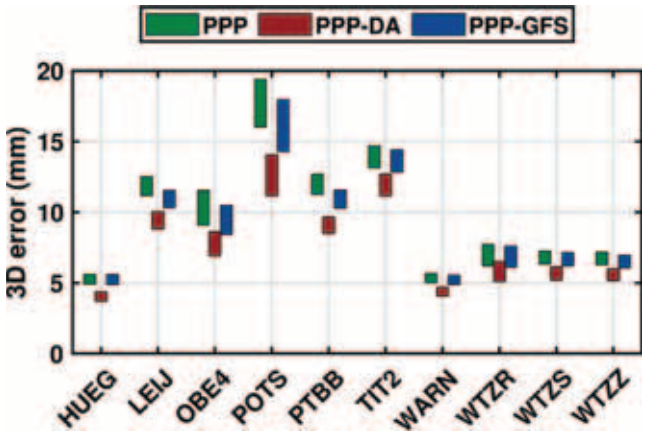
PPP
PPP-DA
PPP-GFS
3D error (mm)
20
15
10
5
0
HUEG
LEIJ
OBE4
POTS
PTBB
TIT2
WARN
WTZR
WTZS
WTZZ

Figure 17.

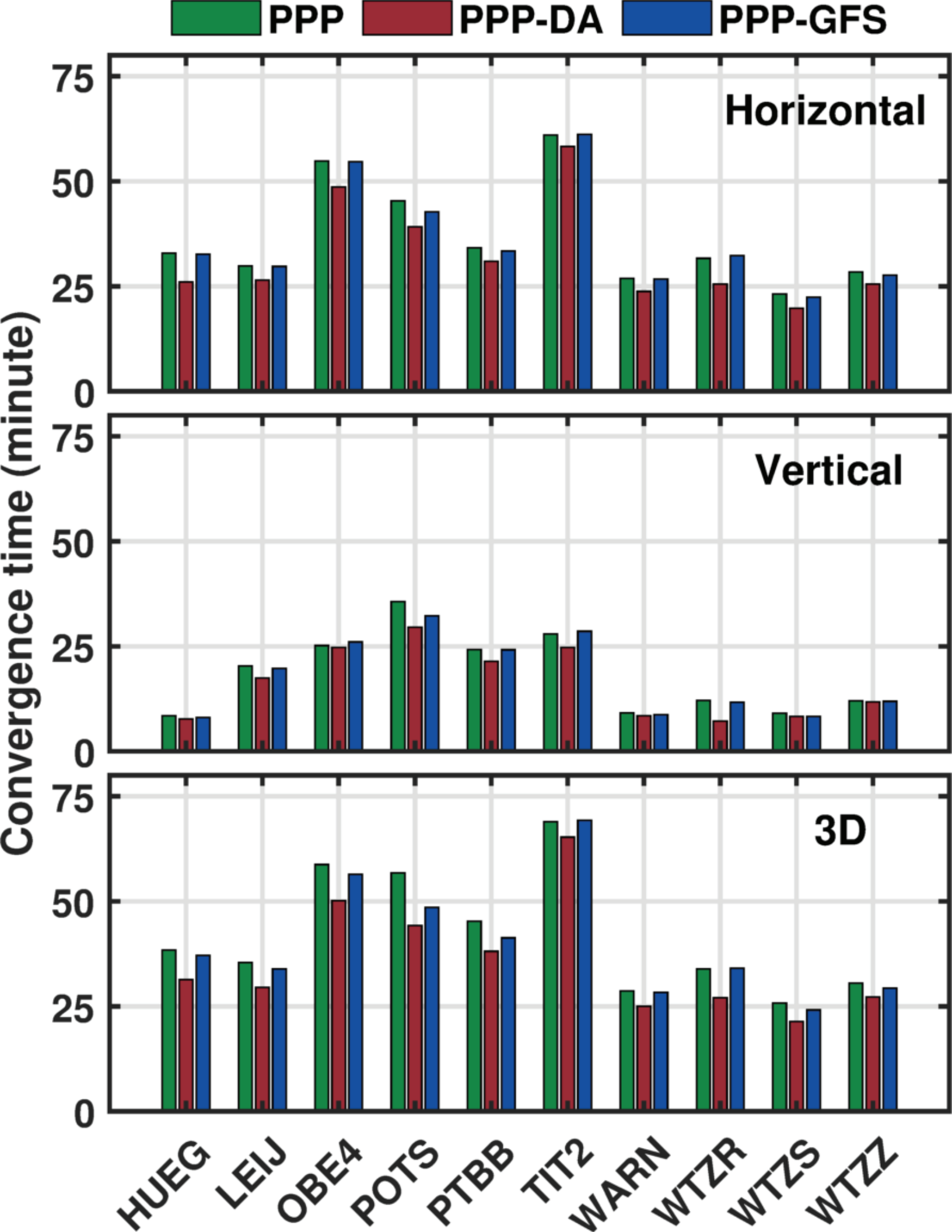
PPP
PPP-DA
PPP-GFS
Horizontal
Vertical
3D
Convergence time (minute)
0
25
50
75
HUEG
LEIJ
OBE4
POTS
PTBB
TIT2
WARN
WTZR
WTZS
WTZZ

Figure 18.

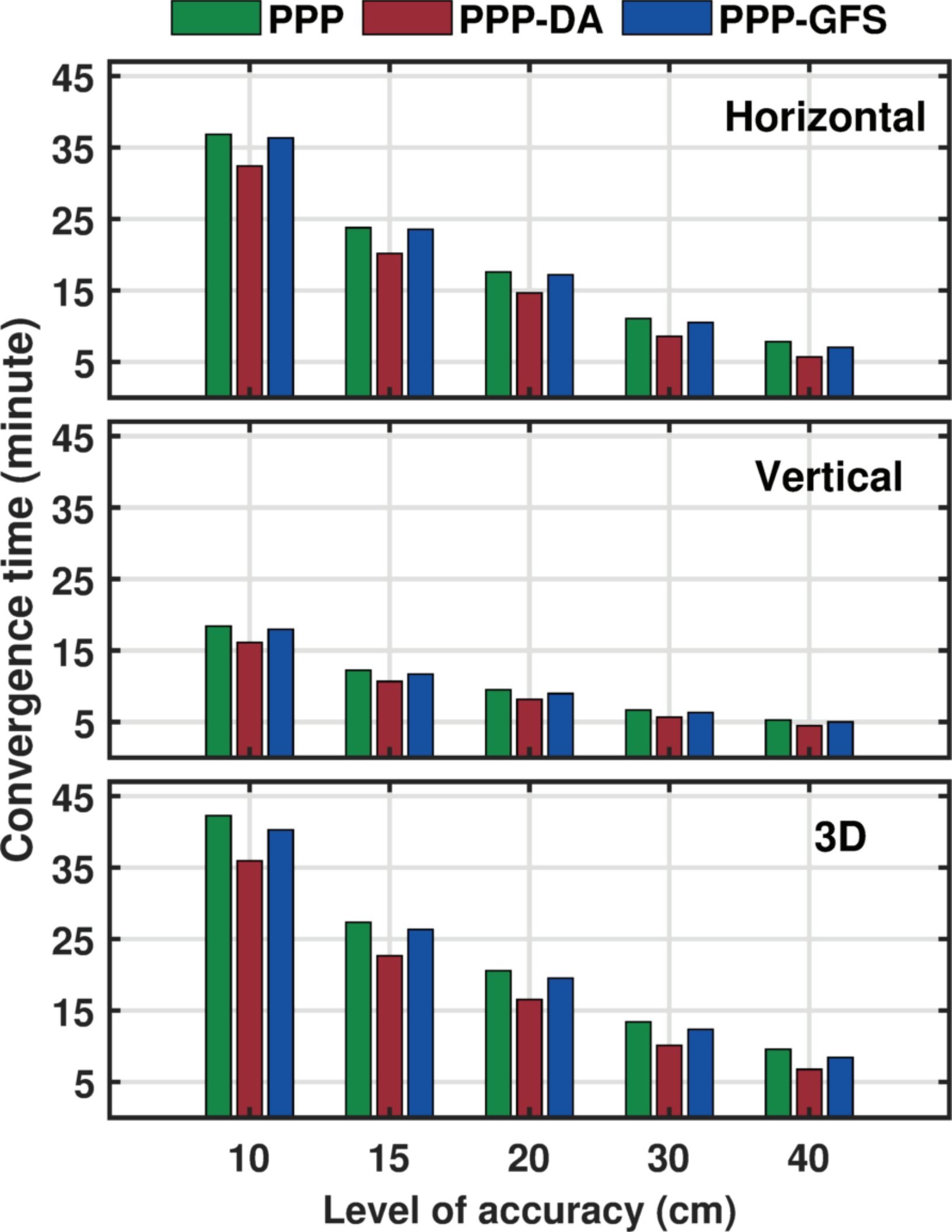
PPP
PPP-DA
PPP-GFS
Horizontal
Vertical
3D
45
35
25
15
5
Convergence time (minute)
10
15
20
30
40
Level of accuracy (cm)

Figure 19.

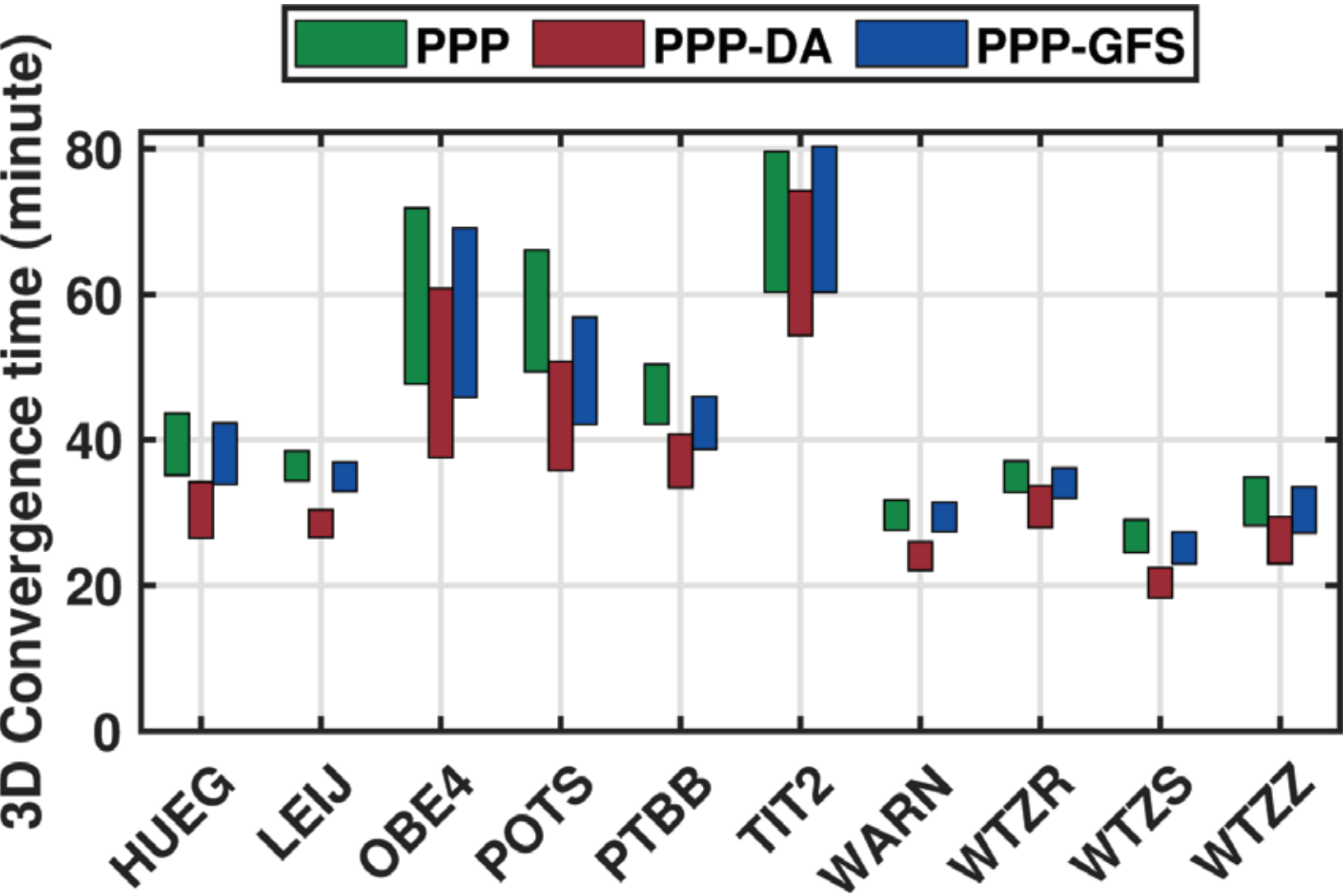
PPP
PPP-DA
PPP-GFS
3D Convergence time (minute)
0
20
40
60
80
HUEG
LEIJ
OBE4
POTS
PTBB
TIT2
WARN
WTZR
WTZS
WTZZ